

Master's thesis

**Measurement of  $\omega$  and  $\phi$  meson production via dimuons  
at forward rapidity in  $pp$  collisions at  $\sqrt{s} = 13.6$  TeV  
with ALICE**

Author : Masahiro Oida

Supervisor : Prof. Kenta Shigaki

Co-Examiner :

Hiroshima University  
Graduate School of Advanced Science and Engineering  
Physics program

Affiliation : Quark Physics Laboratory and SKCM<sup>2</sup>

# Contents

<b>1</b>	<b>Introduction</b>	<b>1</b>
1.1	QCD . . . . .	1
1.2	Chiral symmetry . . . . .	2
1.3	NJL model . . . . .	3
1.4	Quark-Gluon Plasma . . . . .	5
1.5	Heavy Ion collision . . . . .	5
1.6	Dilepton Measurement . . . . .	7
1.7	Search for chiral symmetry restoration in QGP . . . . .	8
1.8	Analysis of pp collision data as a baseline . . . . .	8
<b>2</b>	<b>Detector setup</b>	<b>10</b>
2.1	Large Hadron Collider . . . . .	10
2.2	A Large Ion Collider Experiment . . . . .	10
2.2.1	MUON Spectrometer . . . . .	11
2.2.2	MFT . . . . .	11
2.2.3	MFT-MUON Track Matching . . . . .	12
<b>3</b>	<b>Analysis</b>	<b>12</b>
3.1	DataSet . . . . .	12
3.2	Event selection . . . . .	12
3.3	Single muon track reconstruction . . . . .	13
3.4	Single muon selection . . . . .	13
3.5	Dimuon analysis . . . . .	13
3.5.1	Dimuon reconstruction . . . . .	13
3.5.2	Combinatorial background subtraction . . . . .	14
3.5.3	Peak extraction of $\omega \rightarrow \mu\mu, \phi \rightarrow \mu\mu$ . . . . .	17
3.5.4	Yield calculation of $\omega, \phi$ . . . . .	19
3.6	Analysis for improving MFT-MCH matching purity . . . . .	20
3.6.1	MFT-MCH matching $\chi^2$ optimization . . . . .	21
3.6.2	Fake match track removal analysis of Global Track using MFT Track $\eta$ - MCH Track $\eta$ . . . . .	24
<b>4</b>	<b>Results and Discussion</b>	<b>29</b>
<b>5</b>	<b>Summary</b>	<b>30</b>
<b>6</b>	<b>Acknowledgements</b>	<b>30</b>

## Abstract

As theoretically explained, hadrons that constitute matter acquire mass dynamically through spontaneous chiral symmetry breaking. The degree of chiral symmetry breaking is expressed by the expectation value of quark condensate ( $\langle q\bar{q} \rangle$ ). Since  $\langle q\bar{q} \rangle$  approaches zero in ultra-high temperature and high-density regions, chiral symmetry restoration is expected. Consequently, hadron mass changes are also considered to occur. When quarks and gluons reach an ultra-high temperature and high-density state, a phase transition from the hadron phase to the quark-gluon plasma (QGP) phase occurs. QGP can be created through high-energy heavy-ion collision experiments. In other words, chiral symmetry restoration is expected within QGP, which is generated by high-energy heavy-ion collisions. Light vector mesons are theoretically predicted to exhibit significant mass distribution changes. So far, searches for mass modifications of light vector mesons ( $\rho, \omega, \phi$ ) inside QGP have been conducted using lepton pairs. Light vector mesons serve as probes for hadron mass within QGP. They decay exclusively into lepton pairs, which do not strongly interact with QGP. Additionally, due to their relatively short lifetimes, they tend to decay inside QGP at low transverse momentum, providing information on hadron mass within QGP. However, the observed changes in the mass distribution of lepton pairs can be explained by mechanisms other than chiral symmetry restoration, and a definitive conclusion has not yet been reached.

Therefore, I aim to investigate chiral symmetry restoration by measuring muon pairs using the forward detector system of the ALICE experiment during LHC Run 3 and clarifying the transverse momentum dependence of light vector meson mass distribution changes in lead nucleus collision events. The forward region of the ALICE experiment is equipped with high-performance detectors for muon identification. Unlike electron pairs, muon pairs are not produced from  $\pi^0$  Dalitz decays and their contribution from photon ( $\gamma$ ) conversions into electron pairs in materials is minimal. Thus, muon pair measurements offer a better signal-to-background ratio than electron pair measurements. In Run 3, a new silicon detector (MFT) was installed into the ALICE forward detector system. This enables precise measurement of muon production points and improves the accuracy of pseudo-rapidity and azimuthal angle measurements. The MFT is expected to enhance the removal of heavy-flavour muons based on their different lifetimes, improve low transverse momentum measurement accuracy, and increase the mass resolution of muon pairs.

This master's thesis presents the transverse momentum dependence of  $\omega, \phi$  mesons yield using forward muon pairs in proton collision events from ALICE Run 3. Proton collision analysis serves as a reference for lead nucleus collision analysis. Additionally, it plays a crucial role in evaluating and improving the new muon track reconstruction with the MFT. Track reconstruction was performed using the forward muon tracking detector system (MFT-MCH-MID), and the invariant mass distribution of muon pairs was reconstructed. A fit was applied to the extracted  $\omega, \phi$  meson peaks and their yields were calculated. The transverse momentum dependence of these yields was then determined. Along with this analysis, optimization of the matching  $\chi^2$  cut between MFT and MCH tracks was conducted to minimize the statistical uncertainty of  $\omega, \phi$  yields under the current track reconstruction quality. Furthermore, an analysis was performed to remove falsely matched tracks in MFT-MCH matching. By optimizing the pseudo-rapidity difference ( $\Delta\eta$ ) cut between MFT and MCH tracks constituting a reconstructed track in the MFT-MCH-MID system, the  $\Delta\eta$  value that effectively removes fake match tracks was determined.

# 1 Introduction

## 1.1 QCD

The fundamental components of the matter around us are elementary particles. The behaviour of elementary particles, such as quarks and gluons, is described by quantum field theory. In particular, quarks and gluons possess degrees of freedom called color, the physics governing this degree of freedom is known as Quantum Chromodynamics (QCD). QCD is based on an SU(3) gauge theory and describes the strong interaction. The QCD Lagrangian is expressed as follows:

$$\mathcal{L}_{QCD} = \sum_q \bar{\psi}_{q,a} (i\gamma^\mu \partial_\mu - m_q) \psi_{q,a} + g_s \sum_q \bar{\psi}_{q,a} \gamma^\mu T_{ab}^A \psi_{q,b} G_\mu^A - \frac{1}{4} G_{\mu\nu}^A G^{A\mu\nu} \quad (1)$$

$\psi_{q,a}$  and  $\bar{\psi}_{q,a}$  represent the quark and antiquark fields, where  $q$  denotes the flavor degree of freedom, and  $a$  denotes the color degree of freedom.  $\gamma^\mu$  is the gamma matrices,  $m_q$  is the quark mass corresponding to each flavor,  $g_s$  is the QCD coupling constant,  $T_{ab}^A$  are the generator matrices,  $G_\mu^A$  is the gluon field, and  $G_{\mu\nu}^A$  is the gluon field tensor.

The first term in (1) represents the term for a free particle of mass  $m$ , the second term represents the interaction between quarks and gluons, and the third term represents the interaction between gluons themselves. A significant difference from Quantum Electrodynamics (QED), which describes electromagnetic interactions, is the presence of the coupling constant  $\alpha_s(Q^2)$  and the self-interaction of the gluon field. In QED, the coupling constant does not depend on the energy scale. However, the coupling constant  $\alpha_s(Q^2)$  that appears in QCD depends on the energy scale. Figure 1 shows how

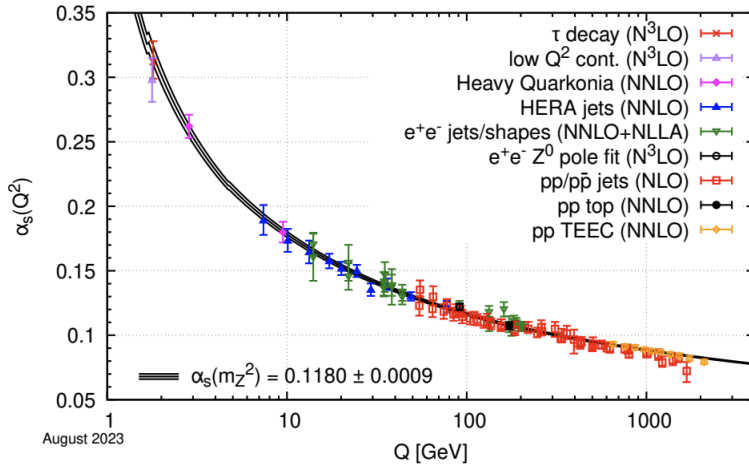


Figure 1:  $Q^2$  dependence of QCD coupling constants

the coupling constant  $\alpha_s(Q^2)$  changes with the energy scale[1]. The coupling constant becomes small at high energy scales, corresponding to short distances. This reflects the phenomenon of asymptotic freedom, where quarks behave as free particles when they are sufficiently close to each other. On the other hand, at low energy scales corresponding to long distances, the coupling constant grows infinitely large. This represents the phenomenon of quark confinement, where quarks cannot be isolated as individual particles.

Next, we focus on gluon selfinteraction. The gluon field tensor is expressed as:

$$G_{\mu\nu}^A = \partial_\mu G_\nu^A - \partial_\nu G_\mu^A + g_s f^{ABC} G_\mu^B G_\nu^C \quad (2)$$

where  $f^{ABC}$  are the structure constants of the SU(3) group. Substituting this into the third term of (1), we obtain:

$$\begin{aligned} -\frac{1}{4}G_{\mu\nu}^A G^{A\mu\nu} &= -\frac{1}{4}(\partial_\mu G_\nu^A - \partial_\nu G_\mu^A + g_s f^{ABC} G_\mu^B G_\nu^C)(\partial^\mu G^{A\nu} - \partial^\nu G^{A\mu} + g_s f^{ABC} G^{B\mu} G^{C\nu}) \\ &= -\frac{1}{4}(\partial_\mu G_\nu^A - \partial_\nu G_\mu^A)(\partial^\mu G^{A\nu} - \partial^\nu G^{A\mu}) \\ &\quad - g_s f^{ABC} G_\mu^B G_\nu^C \partial^\mu G^{A\nu} - g_s^2 f^{ABE} f^{CDE} G_\mu^A G_\nu^B G^{C\mu} G^{D\nu} \end{aligned} \quad (3)$$

In (3), the first term represents the free gluon field without interactions. The second term represents interactions involving three gluon fields, representing reactions such as  $g + g \rightarrow g$ . The third term corresponds to interactions involving four gluon fields, representing reactions such as  $g + g \rightarrow g + g$ . For photons, the third term in (2) does not exist, so the second and third terms in (3) do not appear. This is because gluons interact with each other due to their color degrees of freedom, which gives rise to gluon selfinteraction.

These characteristics—namely, the coupling constant's energy dependence and the gluons' selfinteraction—contribute to the complex structure of the quark-gluon interactions.

## 1.2 Chiral symmetry

The quark field can be separated into its right-handed and left-handed components. The projection operators for the right-handed and left-handed components are defined as  $P_R$  and  $P_L$ , respectively. Using the  $\gamma_5 = i\gamma_0\gamma_1\gamma_2\gamma_3$  matrices, they are expressed as follows:

$$P_R = \frac{1 + \gamma_5}{2}, \quad P_L = \frac{1 - \gamma_5}{2} \quad (4)$$

(4) hold for these projection operators.

$$P_R + P_L = 1, \quad P_R P_L = 0, \quad P_R^2 = P_R, \quad P_L^2 = P_L \quad (5)$$

The right-handed quark field  $q_R$  and the left-handed quark field  $q_L$  are expressed using the projection operators as follows:

$$q_R = P_R q, \quad q_L = P_L q \quad (6)$$

These components are applied to the QCD Lagrangian:

$$\mathcal{L}_{QCD} = \sum_q \bar{q}(i\gamma^\mu D_\mu - m)q \quad (7)$$

- Kinetic Term (First Term of the QCD Lagrangian)

$$\bar{q}(i\gamma^\mu D_\mu)q = \bar{q}(i\gamma^\mu D_\mu)(P_R^2 + P_L^2)q \quad (8)$$

$$= \bar{q}P_L(i\gamma^\mu D_\mu)P_R q + \bar{q}P_R(i\gamma^\mu D_\mu)P_L q \quad (9)$$

$$= \bar{q}_R(i\gamma^\mu D_\mu)q_R + \bar{q}_L(i\gamma^\mu D_\mu)q_L \quad (10)$$

- Mass Term (Second Term of the QCD Lagrangian)

$$\bar{q}m q = \bar{q}m(P_R^2 + P_L^2)q \quad (11)$$

$$= \bar{q}P_R m P_R q + \bar{q}P_L m P_L q \quad (12)$$

$$= \bar{q}_L m q_R + \bar{q}_R m q_L \quad (13)$$

From the above, the kinetic term of the quark field can be separated into the right-handed and left-handed quark fields, thereby preserving chiral symmetry. However, the mass term mixes the right-handed and left-handed quark fields, breaking chiral symmetry. Considering the chiral limit ( $m_q = 0$ ), the QCD Lagrangian preserves chiral symmetry.

The quark represents the order parameter for the spontaneous breaking of chiral symmetry condensate  $\langle \bar{q}q \rangle$ . As shown in Figure 2[2], this quantity takes a finite value in the ground state of hadrons at standard temperature and density. But, it is expected to approach  $\langle \bar{q}q \rangle \sim 0$  at extremely high temperatures and densities.

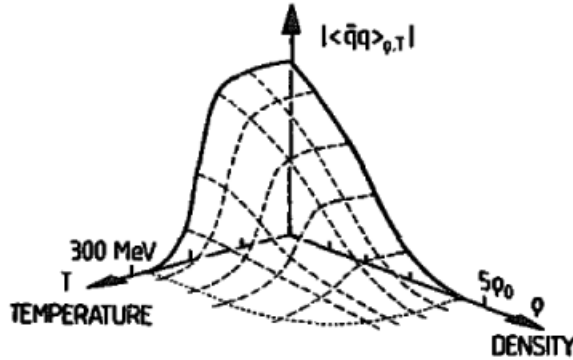


Figure 2: Temperature and density dependence of the expected value of quark condensation

Since the vacuum expectation value of the quark condensate cannot be directly measured, as described later, various other probes are used to investigate the restoration of chiral symmetry.

### 1.3 NJL model

The interaction between quarks and gluons, as described in 1.1, exhibits a complex structure, making it difficult to understand various phenomena from first-principle calculations. Therefore, models are employed to describe various phenomena. One such model is the Nambu-Jona-Lasinio (NJL), an chiral effective model. Its Lagrangian is expressed as follows.

$$\mathcal{L} = \bar{q}i\gamma \cdot \partial q - (-g)[(\bar{q}q)^2 + (\bar{q}i\gamma_5 q)^2] \quad (14)$$

where,  $q$  and  $\bar{q}$  represent quark and antiquark fields, respectively;  $\gamma$  and  $\gamma_5$  are gamma matrices, with  $\gamma_5 = i\gamma_0\gamma_1\gamma_2\gamma_3$ . Since there is an attractive force between quarks and antiquarks, the coupling constant  $g$  is positive and has a dimension of [mass] $^{-2}$ . This model is an effective chiral theory for QCD at the energy scale of 1 GeV. To determine the ground state of this Lagrangian, the self-consistent mean field approximation (MFA) is employed:

$$\langle \bar{q}q \rangle \equiv \frac{-m_0^2\sigma}{G} \quad (15)$$

$$\langle \bar{q}i\gamma_5 q \rangle \equiv \frac{-m_0^2\pi}{G} \quad (16)$$

By substituting (15) and (16) into (14), the expression is reformulated. Defining  $\sigma = \bar{q}q$ ,  $\pi = \bar{q}i\gamma_5 q$ , and  $2g = (G/m_0)^2$ , we get:

$$\mathcal{L}_{MFA} = \bar{q}[i\gamma \cdot \partial - G(\sigma + i\pi\gamma_5)]q - \frac{m_0^2}{2}(\sigma^2 + \pi^2) \quad (17)$$

where, defining  $q_\theta = e^{i\gamma_5 \frac{\theta}{2}} q$ ,  $G\sqrt{\sigma^2 + \pi^2} = M$ , and  $\pi/\sigma = \tan \theta$ , the Hamiltonian can be expressed as follows.  $\theta$  is the parameter of the chiral transformation.

$$H_{MFA} = \int d^3x \left\{ \bar{q}_\theta(x) (-i\gamma \cdot \nabla + M) q_\theta(x) + \frac{m_0^2}{2} \sigma_0^2 \right\} \quad (18)$$

where  $\sigma_0^2 = \sigma^2 + \pi^2$ . Since  $\pi$  is considered sufficiently small, we write  $\sigma$  to  $\sigma_0$ . From this Hamiltonian, the Dirac equation for mass  $M$  can be derived. Its solution is given as 19

$$q_\theta(x) = \frac{1}{\sqrt{V}} \sum_{\mathbf{p}, r=\pm} \sqrt{\frac{M}{E_p}} \left\{ a_M(\mathbf{p}, r) u_M(\mathbf{p}, r) e^{-ip \cdot x} + b_M^\dagger(\mathbf{p}, r) v_M(\mathbf{p}, r) e^{ip \cdot x} \right\} \quad (19)$$

where,  $r$  represents helicity,  $E_p = \sqrt{\mathbf{p}^2 + M^2}$ , and  $M = -g \langle \bar{q}_\theta q_\theta \rangle$ . Next, when  $q_\theta(x)$  is expanded using spinors with zero mass, the solution is:

$$q_\theta(x) = \frac{1}{\sqrt{V}} \sum_{\mathbf{p}, s=R,L} \left\{ a_{\mathbf{p}}^{(s)}(t) u_0(\mathbf{p}, s) e^{-ip \cdot x} + b_{\mathbf{p}}^{(s)\dagger}(t) v_0(\mathbf{p}, s) e^{ip \cdot x} \right\} \quad (20)$$

where  $s$  represents helicity. Using the solutions (19) and (20), the Hamiltonian (18) can be expressed in terms of operators for massive and massless states. Here,  $a_{\mathbf{p}}$  and  $b_{\mathbf{p}}$  are expansion coefficients:

$$\begin{aligned} H_{MFA} &= \sum_{\mathbf{p}, s} \left\{ |\mathbf{p}| \left( a_{\mathbf{p}}^{(s)\dagger}(t) a_{\mathbf{p}}^{(s)}(t) - b_{-\mathbf{p}}^{(s)\dagger}(t) b_{-\mathbf{p}}^{(s)}(t) \right) \right\} \\ &\quad + M \left( b_{-\mathbf{p}}^{(s)}(t) a_{\mathbf{p}}^{(s)}(t) + a_{\mathbf{p}}^{(s)\dagger}(t) b_{-\mathbf{p}}^{(s)\dagger}(t) \right) + V \frac{m_0^2}{2} \sigma_0^2 \end{aligned} \quad (21)$$

$$= \sum_{\mathbf{p}, r} E_p \left( a_M^\dagger(\mathbf{p}, r) a_M(\mathbf{p}, r) - b_M(\mathbf{p}, r) b_M^\dagger(\mathbf{p}, r) \right) + V \frac{m_0^2}{2} \sigma_0^2 \quad (22)$$

From this Hamiltonian, the following Heisenberg equation can be derived:

$$i \begin{pmatrix} \dot{a}_{\mathbf{p}}^{(s)}(t) \\ \dot{b}_{-\mathbf{p}}^{(s)}(t) \end{pmatrix} = \begin{pmatrix} |\mathbf{p}| & M \\ M & -|\mathbf{p}| \end{pmatrix} \begin{pmatrix} a_{\mathbf{p}}^{(s)}(t) \\ b_{-\mathbf{p}}^{(s)}(t) \end{pmatrix} \quad (23)$$

Setting the initial state  $a_{\mathbf{p}}^{(s)}(t=0) = a_{M=0}(\mathbf{p}, s)$ , the solution reveals that the massive and massless operators are connected via the Bogoliubov transformation:

$$\begin{pmatrix} a_M(\mathbf{p}, r) \\ b_M(\mathbf{p}, r)^\dagger \end{pmatrix} = U(\mathbf{p}, r) \begin{pmatrix} a_0(\mathbf{p}, r) \\ b_0(\mathbf{p}, r)^\dagger \end{pmatrix} U^\dagger(\mathbf{p}, r) \quad (24)$$

where  $U(\mathbf{p}, r) = \exp \left\{ -\frac{\theta_p}{2} (a_0^\dagger(\mathbf{p}, r) b_0^\dagger(-\mathbf{p}, r) - b_0(-\mathbf{p}, r) a_0(\mathbf{p}, r)) \right\}$ . The vacuum states for each operator are defined as follows:

$$| \sigma_0 \rangle \rightarrow a_M(\mathbf{p}, r) | \sigma_0 \rangle = b_M(\mathbf{p}, r) | \sigma_0 \rangle = 0 \quad (25)$$

$$| 0 \rangle \rightarrow a_0(\mathbf{p}, r) | 0 \rangle = b_0(\mathbf{p}, r) | 0 \rangle = 0 \quad (26)$$

$a_0(\mathbf{p}, r)^\dagger$  creates an eigenstate of chirality, while  $a_M(\mathbf{p}, r)^\dagger$  creates an eigenstate of helicity. Based on the vacuum definition and (24), acting on  $| 0 \rangle$  produces an eigenstate of helicity but not a definite chirality eigenstate. This implies that "chiral symmetry is spontaneously broken".

Thus, the NJL model theoretically predicts vacuum phase transitions. In our universe, it is believed that quark condensation spontaneously breaks chiral symmetry, leading to hadrons acquiring significant masses.

## 1.4 Quark-Gluon Plasma

When hadrons are exposed to extremely high temperatures and densities, they transition into a plasma state known as the Quark-Gluon Plasma (QGP). In the QGP state, quarks are resolved from confinement, and chiral symmetry restoration is also expected. Furthermore, it is believed that the universe was in a QGP state immediately following the Big Bang. On the QCD phase diagram, which represents the phase structure of quarks and gluons, the QGP phase appears as shown in Figure 3. The QGP phase can be observed in high-temperature regions in both high net baryon density and

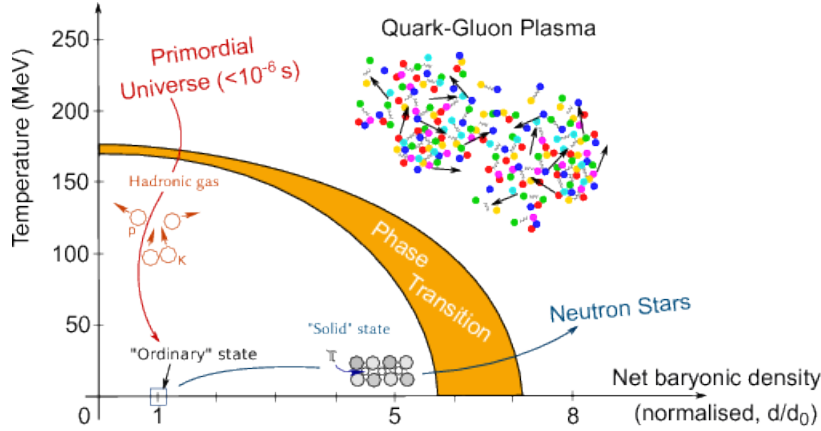


Figure 3: QCD Phase Diagram[3]

low net baryon density areas. Two types of phase transitions are related in the transition to the QGP phase. The first is the chiral phase transition. The second is the deconfinement-confinement phase transition.

The chiral phase transition is the spontaneous breaking of chiral symmetry as the vacuum undergoes a phase transition, allowing quarks to acquire a substantial effective mass. In other words, the chiral phase transition is deeply related to the mass acquisition of hadrons. The deconfinement-confinement phase transition pertains to the confinement of quarks. In the hadronic ground state, quarks are confined by color interaction. However, in the QGP state, quarks are resolved from confinement and transition into a plasma state. This is the deconfinement-confinement phase transition. While these transitions are believed to occur at approximately a similar critical temperature, this relationship is not unsolved, and research is ongoing.

## 1.5 Heavy Ion collision

The existence of QGP, which are ultrahigh-temperature or dense materials, has been confirmed by heavy-ion collision experiments. Figure 4 shows the time evolution proceeds in the following.

1. Pre-equilibrium state
2. QGP
3. Hadronization
4. Kinetic Freeze-out

In the initial stage of the collision, partons from the nucleons undergo elastic and deep inelastic scatterings to reach thermalisation. During this initial collision, phenomena such as jet production

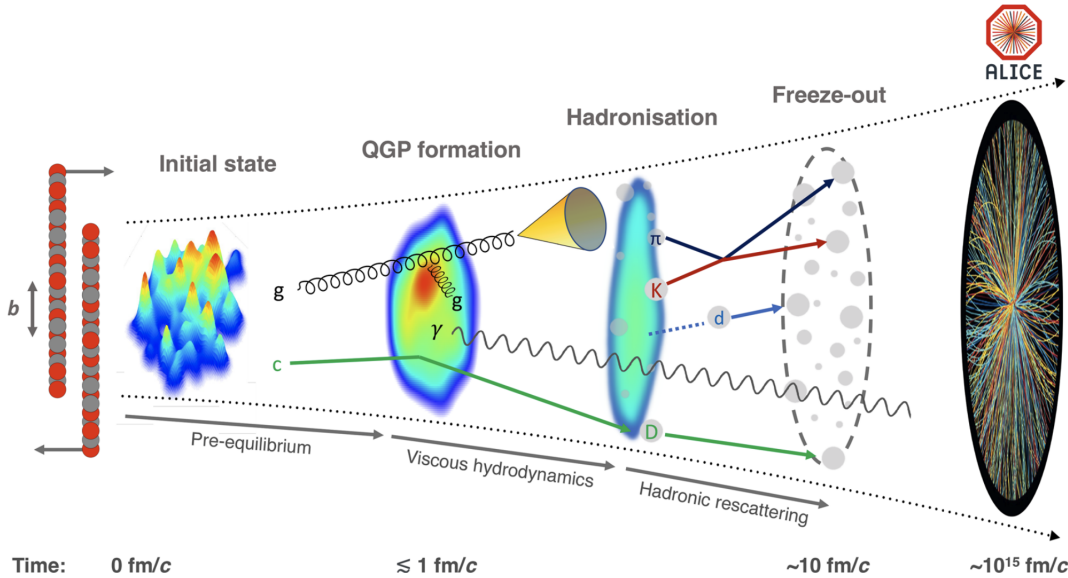


Figure 4: The evolution of a heavy-ion collision at LHC energies[4]

and the pair production of heavy quarks occur. Once the material generated in the collision region reaches thermal equilibrium, the system transitions into the QGP state.

In the QGP state, photons and lepton pairs originating from the thermal radiation of high-temperature matter are generated. Jets interact with the QGP and lose energy, resulting in jet quenching, while heavy quarks undergo deconfinement due to the color Debye screening. Subsequently, as the QGP cools, hadronisation occurs, leading to chemical freeze-out.

Chemical freeze-out refers to stopping changes in particle species due to deeply inelastic scatterings among particles. However, elastic scatterings between hadrons continue, and momentum exchange among particles. Later, kinetic freeze-out occurs, fixing the momenta and other properties of the particles. The particles finally detected are those that remain after the kinetic freeze-out. Thus, QGP is formed during the temporal evolution of heavy-ion collisions, and its lifetime is extremely short.

The QGP generated in heavy-ion collisions has its density and temperature determined by the collision energy. High-density QGP regions are realised at collision energies of  $\sqrt{s_{NN}} \lesssim 10$  [GeV]. At these energies, the colliding particles stop at the collision point. They create a high-density state where kinetic energy is converted directly into heat, increasing the temperature.

On the other hand, high temperature, low net baryon density regions are achieved at collision energies of  $\sqrt{s_{NN}} \gtrsim 100$  [GeV]. In this energy regime, the colliding particles do not stop but pass through each other, producing many pair creations. As a result, the baryon number density does not become large relative to the temperature. However, a high energy density region leads to the creation of high-temperature matter near the collision point.

In the ALICE experiment, LHC Run 3 operations began in 2022, initiating Pb-Pb collision measurements at  $\sqrt{s_{NN}} = 5.36$  TeV. This collision energy produces QGP in the ultrahigh temperature, low net baryon density region. Moreover, compared to the QGP generated at  $\sqrt{s_{NN}} = 200$  GeV at RHIC, the higher collision energy at LHC enables the measurement of a larger QGP than ever before.

## 1.6 Dilepton Measurement

Dilepton measurement is a good probe for investigating the time evolution of heavy-ion collisions. Leptons do not interact with strong interactions, making them less affected by the QGP. This characteristic allows for the measurement of a distribution that sums up dileptons from all stages of heavy-ion collisions. The sources of dilepton production are as Figure 5.

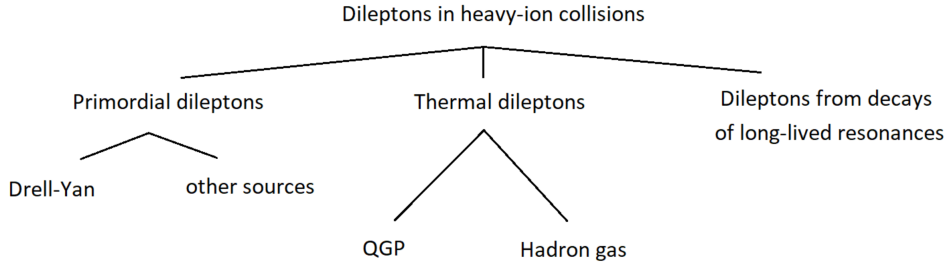


Figure 5: Dilepton source[5]

- Primordial dileptons (from  $q\bar{q}$  annihilation)
- Thermal dileptons
- Dileptons from hadron decays

The dilepton mass regions are associated with the time evolution of heavy ion collisions respectively. In the High-Mass Region, primordial dileptons (Drell-Yan) constitute the continuum component

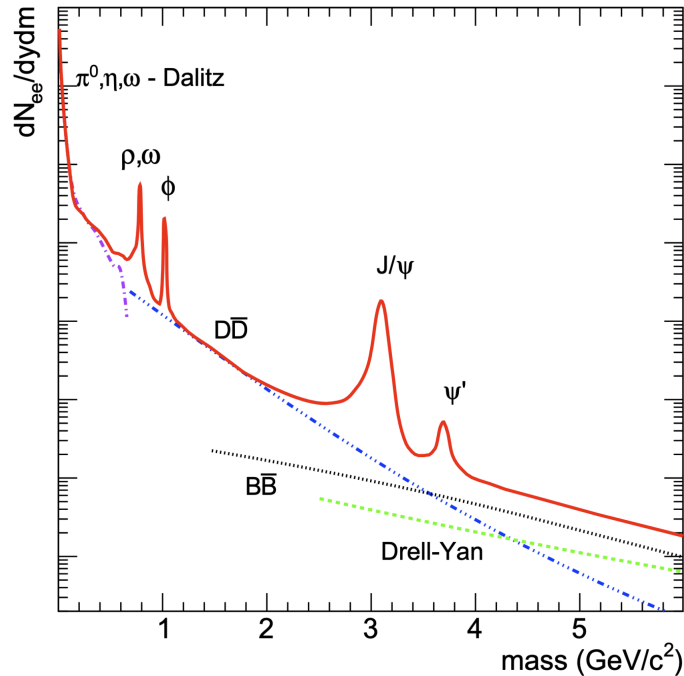


Figure 6: Expected mass spectrum from dileptons[7]

of the mass distribution. It is related to the initial state of the collision. In the Intermediate-Mass

Region, thermal dileptons originating from the QGP and continuum components such as open-charm and open-beauty are observed.

Finally, in the Low-Mass Region, the Dilepton distribution predominantly derives from light meson decays from the hadronic gas. Most dileptons from hadron decays have longer lifetimes than the QGP. So these mesons observed in this region are mostly from the hadron gas. However, light vector mesons ( $\rho, \omega, \phi$ ) have extremely short lifetimes. The effect of the QGP has been suggested.

## 1.7 Search for chiral symmetry restoration in QGP

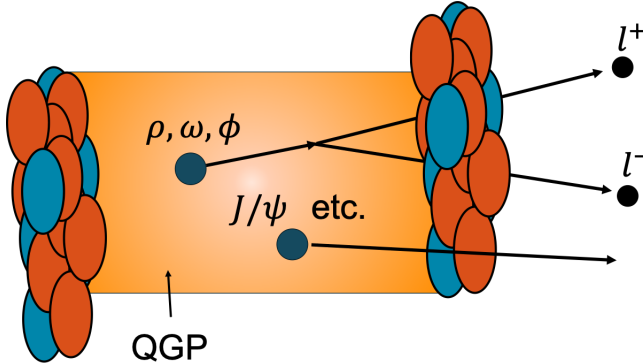


Figure 7: Low mass vector meson decay in QGP

In the QGP, an ultra-high temperature and high-density state are expected to be realised, leading to  $<\bar{q}q> \sim 0$  and restoring chiral symmetry. Light vector mesons ( $\rho, \omega, \phi$ ) serve as probes for the masses of hadrons in the QGP. These particles have short lifetimes and decay channels into dileptons. As shown in Figure 7, their short lifetimes make it possible for them to decay within the QGP, which would otherwise immediately hadronise. Additionally, since they decay exclusively into dileptons, which do not undergo strong interactions with the QGP, the masses of hadrons within the QGP can be measured.

In past experiments, the restoration of chiral symmetry was investigated using dileptons. In the SPS-NA60 experiment, the excess of muon pairs in the low-mass region was reported. However, the excess could also be explained by  $\pi + \pi \rightarrow \rho \rightarrow \pi\pi$ ; thus, it did not serve as definitive evidence of chiral symmetry restoration[8].

Additionally, in the electron pair measurements during ALICE Run 2  $\sqrt{s_{NN}} = 5.02$  TeV PbPb collisions, contributions from open-charm and open-beauty were estimated along with the vacuum dilepton distribution excluding  $\rho$ , and an excess of electron pairs was reported. The excess was explained as thermal dileptons from the QGP within the error range demonstrated[6].

## 1.8 Analysis of pp collision data as a baseline

This paper presents the analysis results of proton-proton collision events. The particles generated in proton-proton collisions are produced from the vacuum. Measurements of collision events where QGP is not produced serve as a baseline for comparison with events where QGP is generated. The quality of track reconstruction is still insufficient, and the muon pair analysis is also incomplete. Furthermore, the quality of muon tracks in heavy-ion collisions is more challenging than in proton-proton collisions due to the large number of particles generated in each event.

The purpose of this study is to provide an analysis as a baseline for future studies of  $\sqrt{s_{NN}} = 5.02$  PbPb collisions, where QGP is expected to be generated and to improve the quality of muon tracks in ALICE Run 3  $\sqrt{s_{NN}} = 13.6$  TeV pp collisions.

## 2 Detector setup

### 2.1 Large Hadron Collider

The Large Hadron Collider (LHC) is the world's largest circular accelerator. Figure 8 shows that the LHC and its major experimental groups are located near Geneva, Switzerland. LHC Run 1 was conducted from 2009 to 2013, and Run 2 occurred from 2015 to 2018. The ongoing Run 3 is scheduled to collect physics data from 2022 to the summer of 2026. During the run, most periods involve proton-proton collision measurements, with heavy-ion collision measurements conducted for about one month each year. The LHC accelerator hosts four major experimental groups: ATLAS, CMS, LHCb, and ALICE.

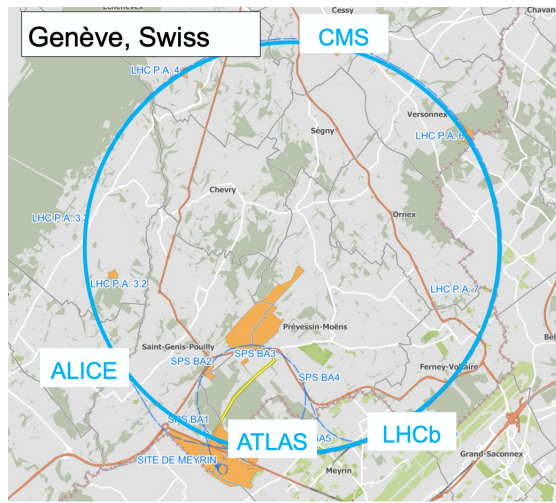


Figure 8: LHC

### 2.2 A Large Ion Collider Experiment

The A Large Ion Collider Experiment (ALICE) collaboration is an international collaboration of 168 research institutions from 40 countries and around 2,000 researchers. The overall view of the ALICE detector is shown in Figure 9. The ALICE detector system is dedicated to research the Quark-Gluon Plasma (QGP) produced in heavy-ion collisions. The detectors can be broadly divided into two main

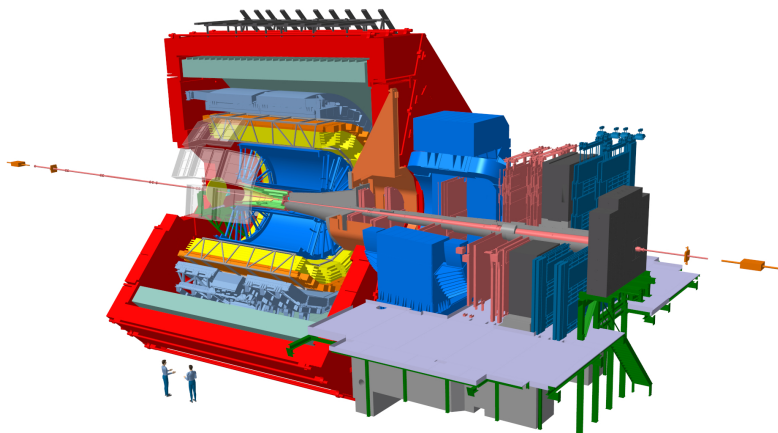


Figure 9: ALICE detectors

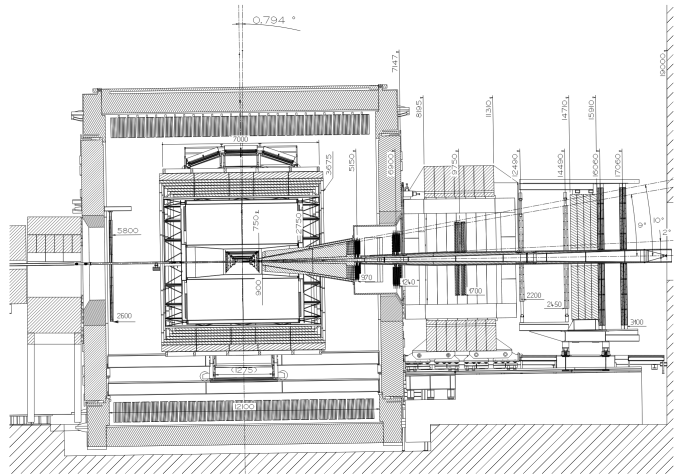


Figure 10: MUON spectrometer

groups: the barrel detector and the forward detector. The barrel detector group includes ITS, TPC, TOF, EMCal, TRD, PHOS/CPV, and HMPID detectors. A magnetic field is applied along the beam axis, bending the motion of charged particles and enabling particle identification, momentum, and energy measurements. The forward detector group is specifically designed for muon measurements and consists of three trackers—MFT, MCH, and MID—and two hadron absorbers. A dipole magnet is placed between MCH, allowing the measurement of muon momentum and sign. Other detectors include ZDC and FIT. The ZDC is placed far from the collision point and measures the number of neutrons and protons, determining the centrality of heavy-ion collision events. The FIT detectors are placed forward and backwards near the collision point to measure the event luminosity and particle multiplicity.

### 2.2.1 MUON Spectrometer

The MUON spectrometer is shown in Figure 10[10]. The MUON spectrometer consists of the Front Absorber, MCH, Iron Wall, and MID and has an acceptance range of  $-4.0 < \eta < -2.5$ . It uses the high penetration power of muons to identify them. Various particles generated at the collision point (IP) pass through the Front Absorber. Hadrons and light electrons, which interact strongly, are absorbed by the Front Absorber. The muons pass through it due to their high penetration power. The muons that pass through the Front Absorber are detected, and any particles such as  $\pi$  mesons produced from interactions within the Front Absorber are measured by the MCH. These particles are absorbed in the Iron Wall, so the MID does not detect them. Therefore, muon identification is performed by combining tracks measured in the MCH and MID. The momentum of the muons is measured using a dipole magnet in the MCH, which is set at a magnetic flux density of  $3.0 \text{ T/m}^2$ .

### 2.2.2 MFT

The MUON spectrometer is shown in Figure 11[9]. The MFT is a newly installed silicon pixel detector between  $z = -46.0$  and  $z = -76.8$  cm with an acceptance range of  $-3.6 < \eta < -2.5$  in Run 3. It consists of 5 layers of disks that detect tracks and reconstruct MFT standalone tracks considering the influence of the L3 magnet, which creates the ALICE central magnetic field. Since the detector is placed in front of the Front Absorber, the tracks measured include muons and various other particles such as  $\pi$  mesons and  $K$  mesons. Combining these tracks with those measured by the

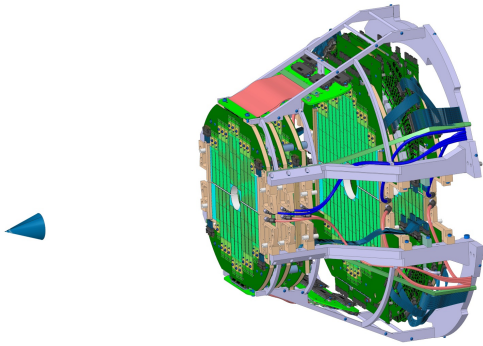


Figure 11: MFT

backward MUON spectrometer makes it possible to measure the *DCA* of the muons. The ability to measure *DCA* enables the separation of muons from *c* and *b* quarks based on differences in lifetime. Additionally, the precision of the opening angle of the muon pair is improved, which enhances mass resolution. Furthermore, since the MFT is placed in front of the Front Absorber, it allows for the measurement of lower transverse momentum muons compared to those measured by the MUON spectrometer alone.

### 2.2.3 MFT-MUON Track Matching

The Global Track was reconstructed using the MCH Track measured with the MUON spectrometer and the MFT Track measured with the MFT. First, the MCH Tracks measured by the MUON spectrometer are extrapolated toward the collision point up to the last disk of the MFT, located at  $z = 76.8$  cm. The extrapolation accounts for multiple scattering and energy loss corrections in the Front Absorber between the MUON spectrometer and MFT. Then, suitable MFT tracks are selected based on both position and direction, and the matching quality is evaluated by comparing the position and slope of the tracks. The best quality MFT track is selected and used to construct the Global Track.

## 3 Analysis

### 3.1 DataSet

The data used is a part of  $pp$  collisions at  $\sqrt{s} = 13.6$  TeV obtained in 2022. The collision rate of  $pp$  is 500 kHz, and the dataset name is LHC22o\_apass7. The Monte Carlo simulation data used in 3.6.2 utilized Pythia8 Monash to reproduce 500 kHz  $pp$  collisions at  $\sqrt{s} = 13.6$  TeV, employing minimum bias event simulations without extracting specific events.

### 3.2 Event selection

The ITS detector system measured the position of the proton-proton collision. The Z-coordinate of the collision point, denoted as  $VtxZ$ , was selected with the condition  $|VtxZ| < 10$  cm, using the ITS centre at  $Z = 0$  as the reference. This cut value is adjusted with the ITS acceptance. The number of events obtained with this cut is  $5.5 \times 10^9$ .

### 3.3 Single muon track reconstruction

The Global Track reconstructed in 2.2.3 was used to calculate the physical quantities of the muon as follows. The MFT Track measures the muon's  $\eta$  and  $\phi$ . The momentum  $p$  was derived by propagating the MCH standalone track to the Z-coordinate of the collision point, with corrections applied for multiple scattering and energy loss in the absorber. For the  $DCA$ , a global fit was performed for all tracks constituting the Global Track, and the resulting track was used. As shown in Figure 12, the track was linearly extrapolated to the Z-coordinate of the collision point (IP), and the distance between the extrapolated point and the collision point was calculated as the  $DCA$ . Similarly, using the same track,  $R_{abs}$  was calculated as the distance from the beam axis at the back edge of the absorber, as shown in Figure 13. Furthermore, the MFT-MCH matching  $\chi^2$  was calculated based on the parameter differences when extrapolating the MFT Track and MCH Track to the matching plane.

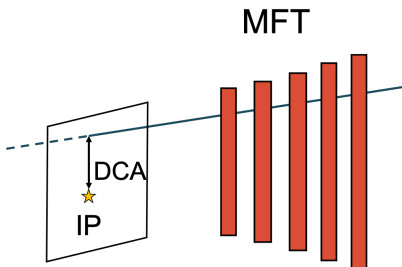


Figure 12: conceptual scheme of  $DCA$

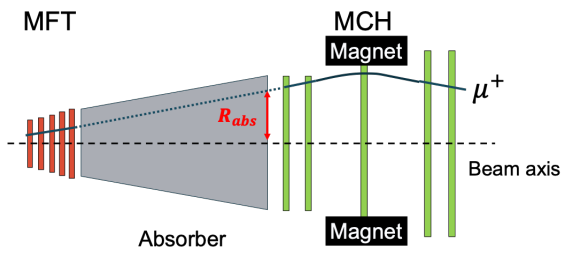


Figure 13: conceptual scheme of  $R_{abs}$

### 3.4 Single muon selection

The cuts applied to the obtained Global Tracks are as follows:

- $-3.6 < \eta < -2.5$
- $17.5 \text{ cm} < R_{abs} < 89.5 \text{ cm}$
- $pDCA < 6\sigma$
- MFT-MCH matching  $\chi^2 < 30$

The  $\eta$  cut is adjusted to match the MFT-MHC-MID acceptance. The cut value of  $R_{abs}$  removes tracks of values where hadron absorbers are not present. The  $pDCA$  is the momentum multiplied by  $DCA$ , and this cut value removes muons derived from the beam gas. The cut was applied at  $6\sigma$  when Gaussian-fitted to the  $pDCA$  distribution. MFT-MCH matching  $\chi^2$  values, optimised to a value that minimises the statistical error of the  $\omega$  and  $\phi$  yield as described below. The final MFT-MCH matching  $\chi^2$  values are obtained from a fit using the points detected when matching MFT and MCH tracks. The values used in this study are optimised to minimise the statistical uncertainty in the  $\omega$  and  $\phi$  yields, as discussed 3.6.1.

### 3.5 Dimuon analysis

#### 3.5.1 Dimuon reconstruction

Dimuons are reconstructed using the single muons selected in 3.4. The mass( $M_{\mu\mu}$ ), transverse-momentum( $p_{T\mu\mu}$ ), pseudorapidity( $\eta_{\mu\mu}$ ), and Azimuth angle( $\phi_{\mu\mu}$ ) of the dimuon are calculated as

(27)~(34). First, the  $p_T$ ,  $\eta$ , and  $\phi$  of the single muons are converted into four-component vectors  $(p_x, p_y, p_z, E)$  using (27),(28),(29),(30).

$$p_x = p_T \cos(\phi) \quad (27)$$

$$p_y = p_T \sin(\phi) \quad (28)$$

$$p_z = p_T \sinh(\eta) \quad (29)$$

$$E = \sqrt{p_T^2 \cosh^2(\eta) + m_\mu^2} \quad (30)$$

Then, using the  $(p_x, p_y, p_z, E)$  of the single muons, the  $(p_{x\mu\mu}, p_{y\mu\mu}, p_{z\mu\mu}, E_{\mu\mu})$  of the dimuon are calculated.

$$\begin{pmatrix} p_{x\mu\mu} \\ p_{y\mu\mu} \\ p_{z\mu\mu} \\ E_{\mu\mu} \end{pmatrix} = \begin{pmatrix} p_{x1} \\ p_{y1} \\ p_{z1} \\ E_1 \end{pmatrix} + \begin{pmatrix} p_{x2} \\ p_{y2} \\ p_{z2} \\ E_2 \end{pmatrix} \quad (31)$$

Using the obtained four-component vector of the dimuon  $(p_{x\mu\mu}, p_{y\mu\mu}, p_{z\mu\mu}, E_{\mu\mu})$ , the pair's  $M_{\mu\mu}$ ,  $p_{T\mu\mu}$ , and  $\eta_{\mu\mu}$  were calculated from the (32),(33),(34).

$$M_{\mu\mu} = \sqrt{E_{\mu\mu}^2 - (p_{x\mu\mu}^2 + p_{y\mu\mu}^2 + p_{z\mu\mu}^2)} \quad (32)$$

$$p_{T\mu\mu} = \sqrt{p_{x\mu\mu}^2 + p_{y\mu\mu}^2} \quad (33)$$

$$\eta_{\mu\mu} = \frac{1}{2} \log \left( \frac{|\vec{p}| + p_{z\mu\mu}}{|\vec{p}| - p_{z\mu\mu}} \right) \quad (34)$$

$$\phi_{\mu\mu} = \arctan \left( \frac{p_y}{p_x} \right) \quad (35)$$

Using (32),(33),(34) and (35), the physical quantities of the dimuon are calculated.

### 3.5.2 Combinatorial background subtraction

The dimuon was reconstructed by pairing oppositely charged muons present in each event. In cases with multiple combinations, all combinations are used to pair the muons and reconstruct the physical quantities of the dimuon. Since all combinations are considered, the mass distribution of uncorrelated muon pairs is also reconstructed. This is called the combinatorial background. This study uses the Like Sign method to subtract the combinatorial background. The Like Sign method is a method that estimates the combinatorial background by using the mass distribution of muon pairs with the same sign from each collision event. The key feature of this method is that it estimates the shape of uncorrelated background events using the like-sign muons from the same event, allowing for the subtraction of mass distributions of weakly correlated particles within each event, such as those arising from elliptic flow in heavy-ion collisions. The estimated uncorrelated background events depend on the  $p_T$  of the dimuon. The calculation formula is given by (36).

$$\frac{dN_{sig}}{dm} = \frac{dN_{same}^{+-}}{dm} - 2R \sqrt{\frac{dN_{same}^{++}}{dm} \frac{dN_{same}^{--}}{dm}} \quad (36)$$

$$2R = \frac{\frac{dN_{mix}^{+-}}{dm}}{\sqrt{\frac{dN_{mix}^{++}}{dm} \frac{dN_{mix}^{--}}{dm}}} \quad (37)$$

Where,  $\frac{dN_{sig}}{dm}$  represents the number of correlated muons at each mass,  $\frac{dN_{same}^{**}}{dm}$  represents the number of same-sign muon pairs in the same event (\*\* corresponds to the muon sign), and  $\frac{dN_{mix}^{**}}{dm}$  represents

the number of muon pairs formed from different events.  $R$  is a term to correct for the acceptance difference due to the muon sign.  $R = 1$  when there is no difference in acceptances by sign. Since muon pairs from different events were not reconstructed in this analysis,  $R = 1$  was used for the calculation.

The result of the combinatorial background subtraction in the dimuon transverse momentum region of  $(1 < p_{T\mu\mu} < 30)$  GeV/c is shown in Figure 14.

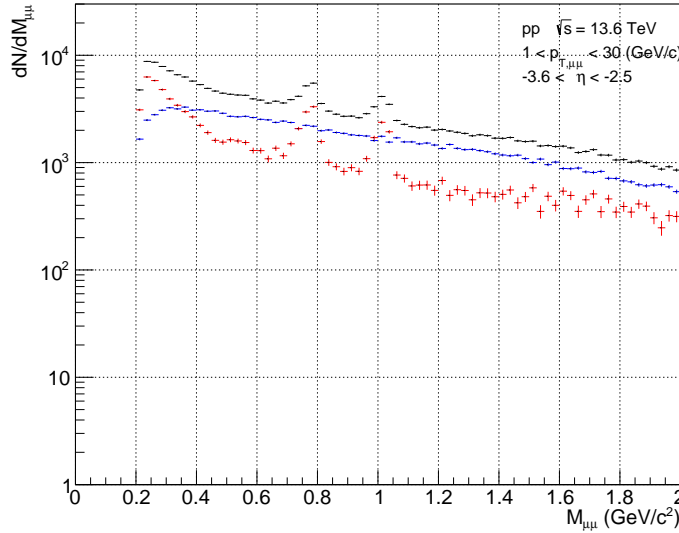


Figure 14: Dimuon invariant mass distribution with transverse momentum  $1 < p_T < 30$  (GeV/c) minus uncorrelated background events. Black is the reconstructed invariant mass distribution for all combinations of muons of different signs in the same event. Blue is the uncorrelated background event estimated using the Like Sign method. Red is the correlated muon vs invariant mass distribution obtained by subtracting blue from black.

The horizontal axis shows the invariant mass, and the vertical axis shows the number of dimuons for each mass bin. The black distribution represents the invariant mass reconstructed by pairing oppositely charged muon particles from all combinations within the same event, while the blue distribution represents the uncorrelated background events estimated using the Like Sign method. The red distribution, obtained by subtracting the blue from the black one, represents the dimuon invariant mass distribution with correlations. The mass distributions were separated by dimuon  $p_{T\mu\mu}$ , and uncorrelated background events were subtracted using the Like Sign method in each invariant mass distribution to examine the transverse momentum dependence of the  $\omega$  and  $\phi$  yields. The subtracted plots are shown in Figure 15.

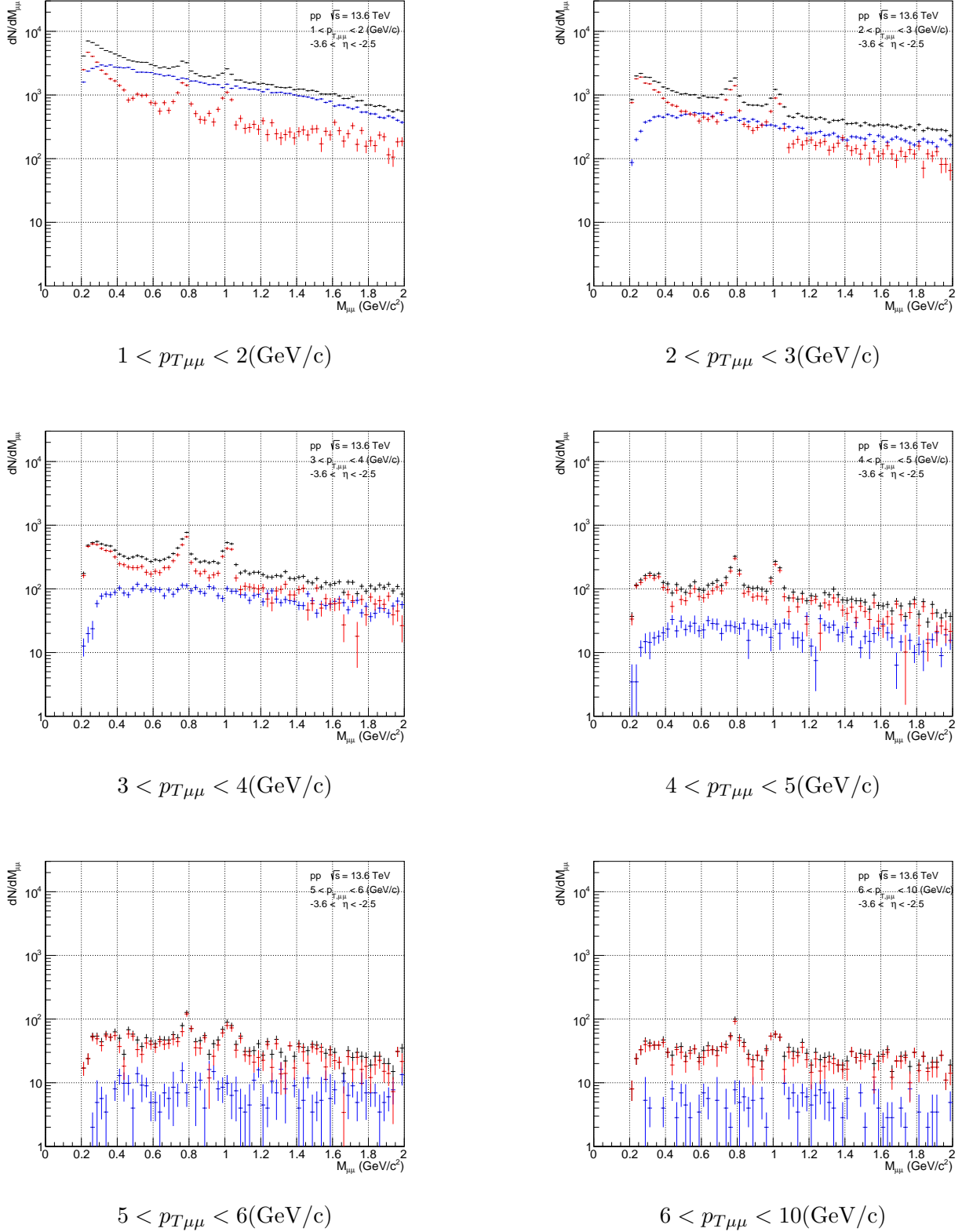


Figure 15: Dimuon invariant mass distribution subtracting each dimuon transverse momentum uncorrelated background event. Black is the reconstructed invariant mass distribution for all combinations of muons of different signs in the same event. Blue is the uncorrelated background event estimated using the Like Sign method. Red is the correlated muon vs invariant mass distribution obtained by subtracting blue from black.

In the region of  $0 < p_T \mu\mu < 1$  GeV, no peaks for  $\omega$  and  $\phi$  were observed. The reason is believed to

be the insufficient resolution of the single muon  $p_T$  and the dominance of tracks with incorrect MFT-MCH matching. The region of  $6 < p_{T\mu\mu} < 10$  GeV was chosen to be wider than other transverse momentum regions to preserve the statistical significance.

### 3.5.3 Peak extraction of $\omega \rightarrow \mu\mu, \phi \rightarrow \mu\mu$

The distributions of the correlated dimuon invariant mass obtained from 3.5.2 are used to extract the distributions of  $\omega \rightarrow \mu\mu$  and  $\phi \rightarrow \mu\mu$ . The dimuon invariant mass distribution under  $2(\text{GeV}/c^2)$  contains pairs of muons coming from light and open heavy-flavor mesons. Charm( $c$ ) and bottom( $b$ ) quarks have heavy masses produced through pair creation in the initial collision. The pair-created  $c\bar{c}$  quarks separate and form  $D\bar{D}$  mesons. The  $D$  and  $\bar{D}$  mesons undergo semileptonic decays, such as  $D \rightarrow \bar{K}^0 + \mu^+ + \nu_\mu$  or  $D \rightarrow \mu^+ + \nu_\mu$ , and  $\bar{D} \rightarrow K^0 + \mu^- + \nu_\mu$  or  $\bar{D} \rightarrow \mu^- + \nu_\mu$ . Since the parent  $D$  and  $\bar{D}$  mesons are produced through pair creation, they are strongly correlated, and their decay products, the muons, also exhibit correlation. As a result, the dimuon mass distribution with correlations is included. The same correlation applies in the case of  $B$  mesons.

- $\eta \rightarrow \mu^+ \mu^-$
- $\eta \rightarrow \mu^+ \mu^- \gamma$
- $\rho \rightarrow \mu^+ \mu^-$
- $\omega \rightarrow \mu^+ \mu^-$
- $\omega \rightarrow \mu^+ \mu^- \pi^0$
- $\eta' \rightarrow \mu^+ \mu^- \gamma$
- $\phi \rightarrow \mu^+ \mu^-$
- $c\bar{c} \rightarrow D\bar{D} \rightarrow \mu^+ \mu^- + \text{others}$
- $b\bar{b} \rightarrow B\bar{B} \rightarrow \mu^+ \mu^- + \text{others}$

The decays  $\omega \rightarrow \mu\mu$  and  $\phi \rightarrow \mu\mu$  are known to exhibit sharp peak structures from previous lepton pair measurements, forming peaks near  $0.8 \text{ GeV}/c^2$  and  $1.0 \text{ GeV}/c^2$  in the mass distribution. It is known that no sharp peak structures exist for any decays other than the two-body decays of  $\omega$  and  $\phi$ . Therefore, the continuous component was fitted using an exponential function. The fitting was performed in the range of  $0.5 < M_{\mu\mu} < 1.3 \text{ GeV}/c^2$ , excluding the regions with peak structures at  $0.7 < M_{\mu\mu} < 0.86$  and  $0.92 < M_{\mu\mu} < 1.15$ . The continuous component was fitted using the exponential function shown (38).

$$f_{BG}(m) = N_{BG} * \exp\{-p1 * m\} \quad (38)$$

where,  $N_{BG}$  and  $p1$  are the fit parameters. The continuous component mass distribution was subtracted using the results from the fit. Gaussian fits were performed for the  $\omega$  and  $\phi$  in the mass regions  $0.7 < M_{\mu\mu} < 0.86 \text{ GeV}/c^2$  and  $0.92 < M_{\mu\mu} < 1.15 \text{ GeV}/c^2$ , respectively. The fitting function is given by (39) and (40).

$$f_\omega = N_\omega * \exp\left\{-\frac{1}{2}\left(\frac{m - M_\omega}{\sigma_\omega}\right)^2\right\} \quad (39)$$

$$f_\phi = N_\phi * \exp\left\{-\frac{1}{2}\left(\frac{m - M_\phi}{\sigma_\phi}\right)^2\right\} \quad (40)$$

The fit parameters are  $N_\omega, N_\phi, M_\omega, M_\phi, \sigma_\omega, \sigma_\phi$ . Specifically,  $M_\omega$  and  $M_\phi$  correspond to the mean mass positions of  $\omega$  and  $\phi$ , while  $\sigma_\omega$  and  $\sigma_\phi$  correspond to the mass widths. Using the fit parameters obtained from the continuous component and the Gaussian fits for  $\omega$  and  $\phi$ , all functions were combined, and a global fit was performed to extract the mean mass positions and mass widths of  $\omega$  and  $\phi$ . The fit range is  $0.5 < M_{\mu\mu} < 1.3$  GeV/c<sup>2</sup>. The function for the overall fit is given by the (41).

$$f(m) = N_{BG} * \exp\{-p1 * m\} + N_\omega * \exp\left\{-\frac{1}{2}\left(\frac{m - M_\omega}{\sigma_\omega}\right)^2\right\} + N_\phi * \exp\left\{-\frac{1}{2}\left(\frac{m - M_\phi}{\sigma_\phi}\right)^2\right\} \quad (41)$$

The parameters for the overall fit are similarly  $N_{BG}, N_\omega, N_\phi, M_\omega, M_\phi, \sigma_\omega, \sigma_\phi$ . The fit results are shown in Figure 16 and Table 1.

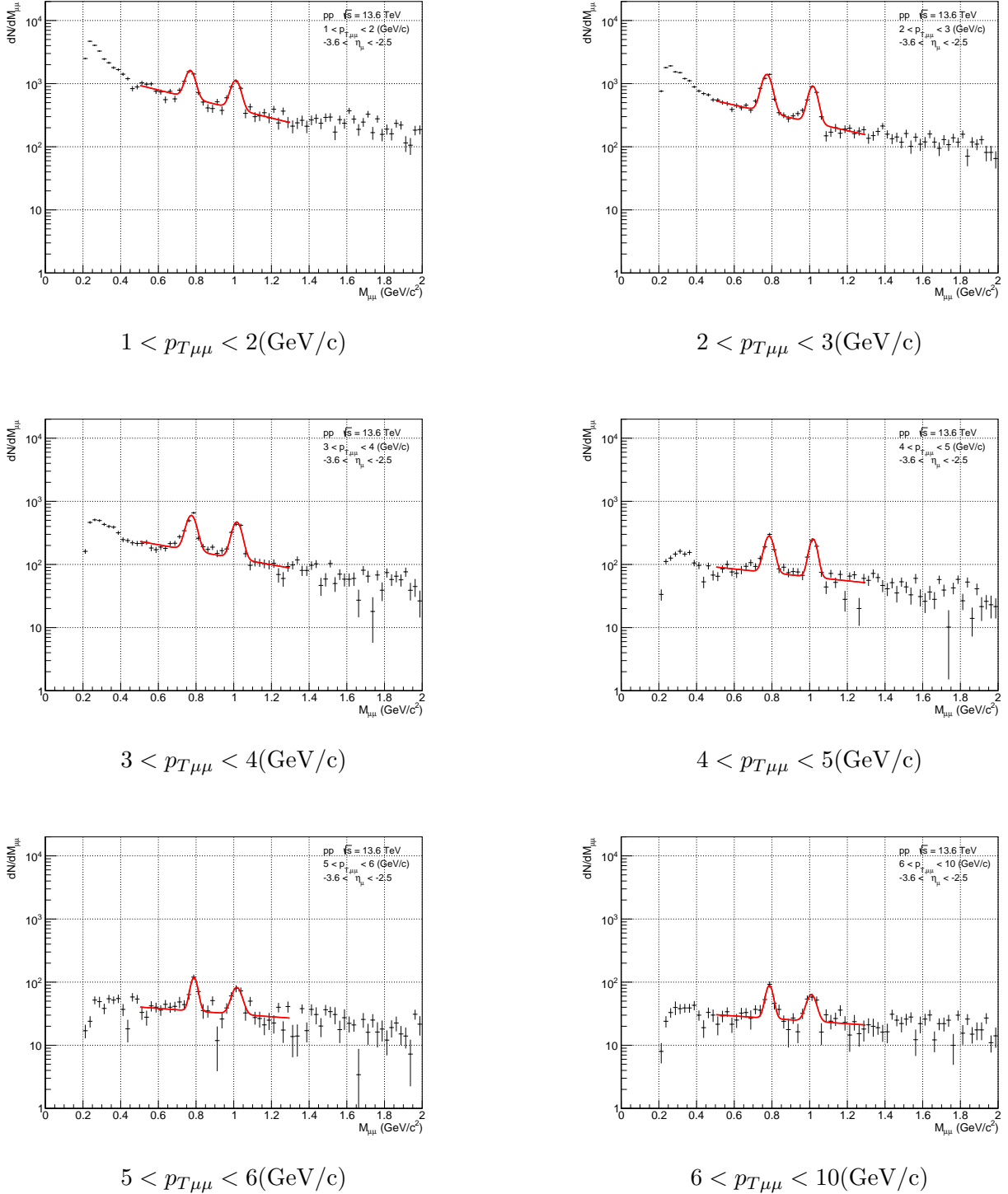


Figure 16: Results of fitting to the correlated invariant mass distribution obtained from Figure 15 in the region  $0.5 < M_{\mu\mu} < 1.3(\text{GeV}/c^2)$ . The red line is the result of the global fit with 41.

The mean mass positions and mass widths of  $\omega$  and  $\phi$  for each transverse momentum, as well as the  $\chi^2$  of the fit, are summarised in the following table.

### 3.5.4 Yield calculation of $\omega, \phi$

The yield for each meson was calculated using the mean mass position and mass width of  $\omega \rightarrow \mu\mu$  and  $\phi \rightarrow \mu\mu$  obtained from the above fit. The number of dimuons falling within  $3\sigma$  of each Gaussian

Table 1: Result of fit at each transverse momentum. mean mass mass width unit is (GeV/c<sup>2</sup>). Unit of transverse momentum is (GeV/c).

	$\omega$ mean mass	$\omega$ mass width	$\phi$ mean mass	$\phi$ mass width	fit $\chi^2$
$1 < p_{T\mu\mu} < 2$	$0.769 \pm 0.002$	$0.025 \pm 0.002$	$1.010 \pm 0.002$	$0.026 \pm 0.002$	47.74/24
$2 < p_{T\mu\mu} < 3$	$0.773 \pm 0.001$	$0.026 \pm 0.001$	$1.017 \pm 0.001$	$0.024 \pm 0.001$	58.80/24
$3 < p_{T\mu\mu} < 4$	$0.775 \pm 0.002$	$0.026 \pm 0.002$	$1.016 \pm 0.002$	$0.025 \pm 0.002$	76.50/24
$4 < p_{T\mu\mu} < 5$	$0.785 \pm 0.002$	$0.024 \pm 0.002$	$1.018 \pm 0.002$	$0.021 \pm 0.002$	53.96/24
$5 < p_{T\mu\mu} < 6$	$0.789 \pm 0.003$	$0.018 \pm 0.003$	$1.016 \pm 0.005$	$0.026 \pm 0.005$	36.85/24
$6 < p_{T\mu\mu} < 10$	$0.786 \pm 0.003$	$0.019 \pm 0.004$	$1.009 \pm 0.005$	$0.024 \pm 0.003$	27.12/24

was calculated as the yield for  $\omega$  and  $\phi$ , respectively.

$$\text{min} = -3 \times \sigma + M \quad (42)$$

$$\text{max} = 3 \times \sigma + M \quad (43)$$

$$\text{Yield} = \sum_{n=\text{min}}^{\text{max}} N_n(m) \quad (44)$$

The yields for each were calculated using the mean mass positions and mass widths of  $\omega \rightarrow \mu\mu$  and  $\phi \rightarrow \mu\mu$  obtained from the above fit. The mass distribution was obtained by subtracting the continuous component from the dimuon mass distribution with correlations. For this mass distribution, the number of entries within three times the mass width from the mass positions of  $\omega$  and  $\phi$  were calculated as their respective yields. The calculation formula is as (44), where the mass distribution after subtracting the continuous component is denoted as  $N_n(m)$ . The results from the

Table 2: Calculated results for  $\omega$  and  $\phi$  yields. The unit of transverse momentum is (GeV/c).

	$\omega$ Yield	$\phi$ Yield
$1 < p_{T\mu\mu} < 2$	$(2.43 \pm 0.18) \times 10^3$	$(1.82 \pm 0.15) \times 10^3$
$2 < p_{T\mu\mu} < 3$	$(2.79 \pm 0.11) \times 10^3$	$(1.64 \pm 0.09) \times 10^3$
$3 < p_{T\mu\mu} < 4$	$(1.278 \pm 0.064) \times 10^3$	$(0.886 \pm 0.055) \times 10^3$
$4 < p_{T\mu\mu} < 5$	$(0.533 \pm 0.038) \times 10^3$	$(0.378 \pm 0.033) \times 10^3$
$5 < p_{T\mu\mu} < 6$	$(0.159 \pm 0.021) \times 10^3$	$(0.142 \pm 0.023) \times 10^3$
$6 < p_{T\mu\mu} < 10$	$(0.033 \pm 0.005) \times 10^3$	$(0.023 \pm 0.004) \times 10^3$

table above are presented as graphs in Figure 35 and Figure 36.

### 3.6 Analysis for improving MFT-MCH matching purity

The mass distribution of dimuons with  $p_{T\mu\mu}$  below 1 (GeV/c<sup>2</sup>), not shown in Figure 15, is presented here. From Figure 17, the peak structures of  $\omega$  and  $\phi$  could not be measured. This is due to the insufficient reconstruction resolution of  $\eta$ ,  $p_T$ , and  $\phi$  at low  $p_T$  for single muons. The introduction of the MFT is expected to enable high-precision measurements of  $\eta$  and  $\phi$ , which would improve the reconstruction resolution of  $p_T$  through enhanced  $\eta$  and  $\phi$  resolution. However, with the current reconstruction method, sufficient resolution has not been achieved, resulting in the inability to observe the peaks of  $\omega$  and  $\phi$  in the dimuon invariant mass distribution at low transverse momentum. This can likely be attributed to issues in matching tracks from the newly introduced MFT and those from the MCH, which prevent achieving adequate resolution. This chapter presents an analysis to improve

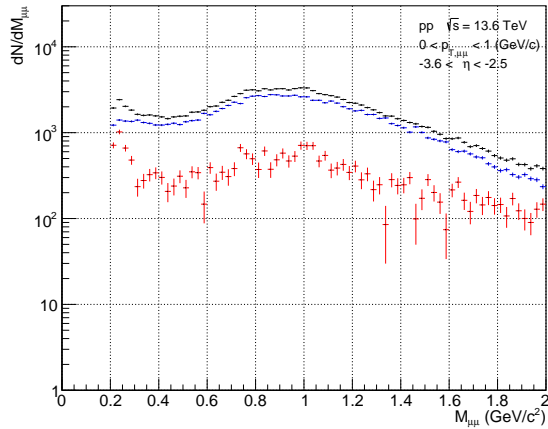


Figure 17: Combinatorial subtraction of dimuon transverse momentum  $0 < p_{T\mu\mu} < 1$ (GeV/c). Black is the reconstructed invariant mass distribution for all combinations of muons of different signs in the same event. Blue is the uncorrelated background event estimated using the Like Sign method. Red is the correlated muon vs invariant mass distribution obtained by subtracting blue from black.

the MFT-MCH matching purity across all transverse momentum distributions without restricting to low  $p_T$ .

### 3.6.1 MFT-MCH matching $\chi^2$ optimization

Using the yield analysis method for  $\omega \rightarrow \mu\mu$  and  $\phi \rightarrow \mu\mu$  described in 3.5.2-3.5.4, the MFT-MCH matching  $\chi^2$  cut value for single muon tracks was optimised to maximise signal detection efficiency. The MFT-MCH matching  $\chi^2$  value represents the parameter difference when extrapolating MFT and MCH tracks to the matching plane. A larger  $\chi^2$  value indicates more fake matches, whereas a smaller value corresponds to more correct matches. Fake match tracks can be removed by applying a cut on this value. However, optimising the cut to minimise fake matches while preserving as many correct matches as possible is necessary. In this study, the optimisation was performed by maximising the signal significance using the peaks of  $\omega$  and  $\phi$ . The signal was calculated by performing the same analysis as in 3.5.2, 3.5.3, and 3.5.4 for the mass distributions in all transverse momentum regions. The number of background events was determined by counting the entries in the background-subtracted mass distribution within the same mass window used for signal calculation, and this was used as the background estimate. The significance,  $S/\sqrt{S+BG}$ , was then calculated. This calculation was performed for mass distributions reconstructed using only muons with an MFT-MCH matching  $\chi^2$  below a given threshold. Figure 18 presents the results of the combinatorial background subtraction after applying the  $\chi^2$  cut. Similar to Figure 15, the black histogram represents the mass distribution reconstructed from all oppositely charged muon pairs in the same event. The blue histogram represents the combinatorial background estimated using the Like Sign method. The red histogram corresponds to the background-subtracted distribution, representing the invariant mass distribution of correlated dimuons.

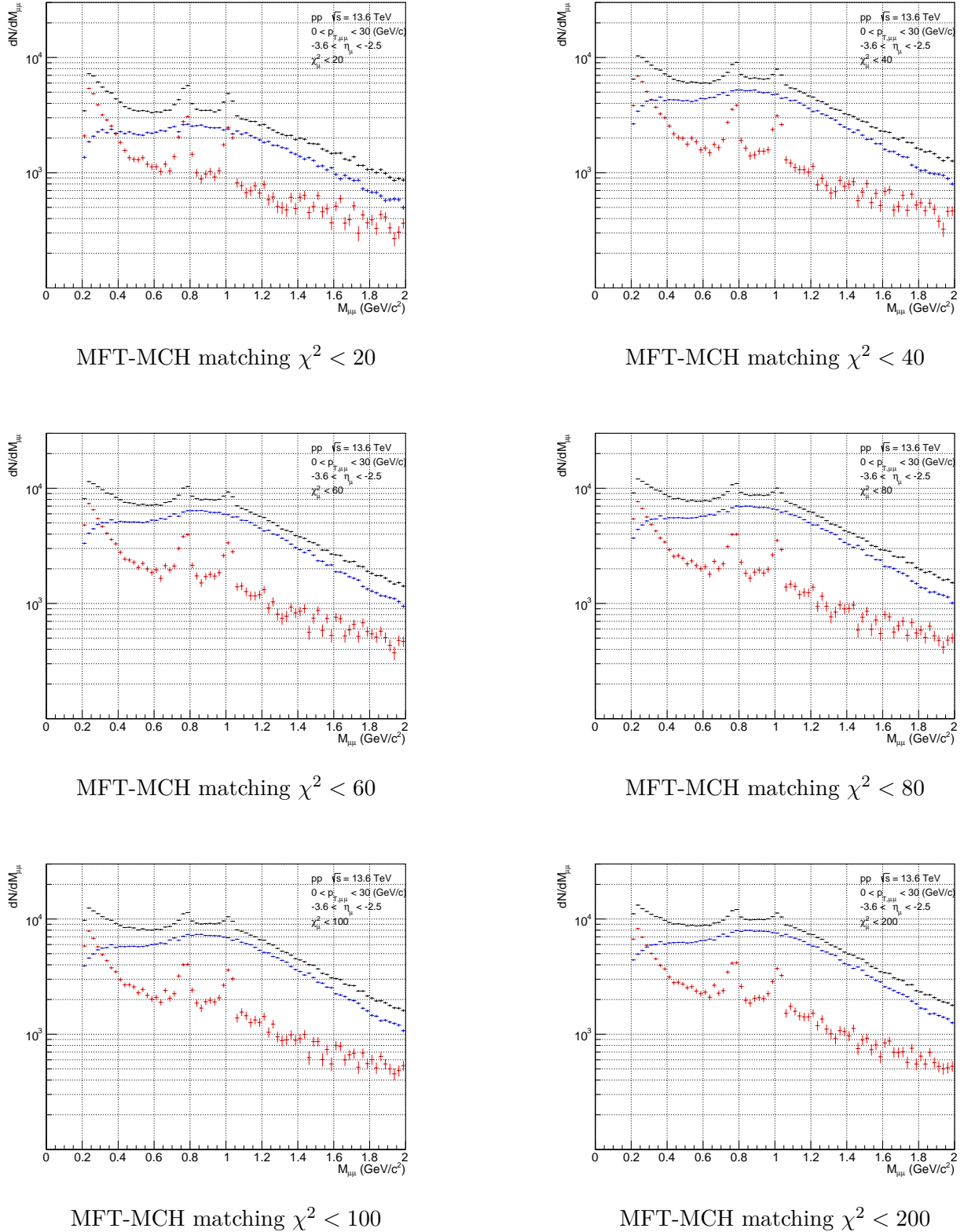


Figure 18: The result of Combinatorial Background subtraction after applying the MFT-MCH matching  $\chi^2$  cut. Black is the reconstructed invariant mass distribution for all combinations of muons of different signs in the same event. Blue is the uncorrelated background event estimated using the Like Sign method. Red is the correlated muon vs invariant mass distribution obtained by subtracting blue from black.

The black distribution decreases in size by reducing the  $\chi^2$  cut. Additionally, it can be observed

that the  $\omega$  and  $\phi$  peaks in the red distribution become more pronounced. Figure 19 shows the fitting results for this red distribution.

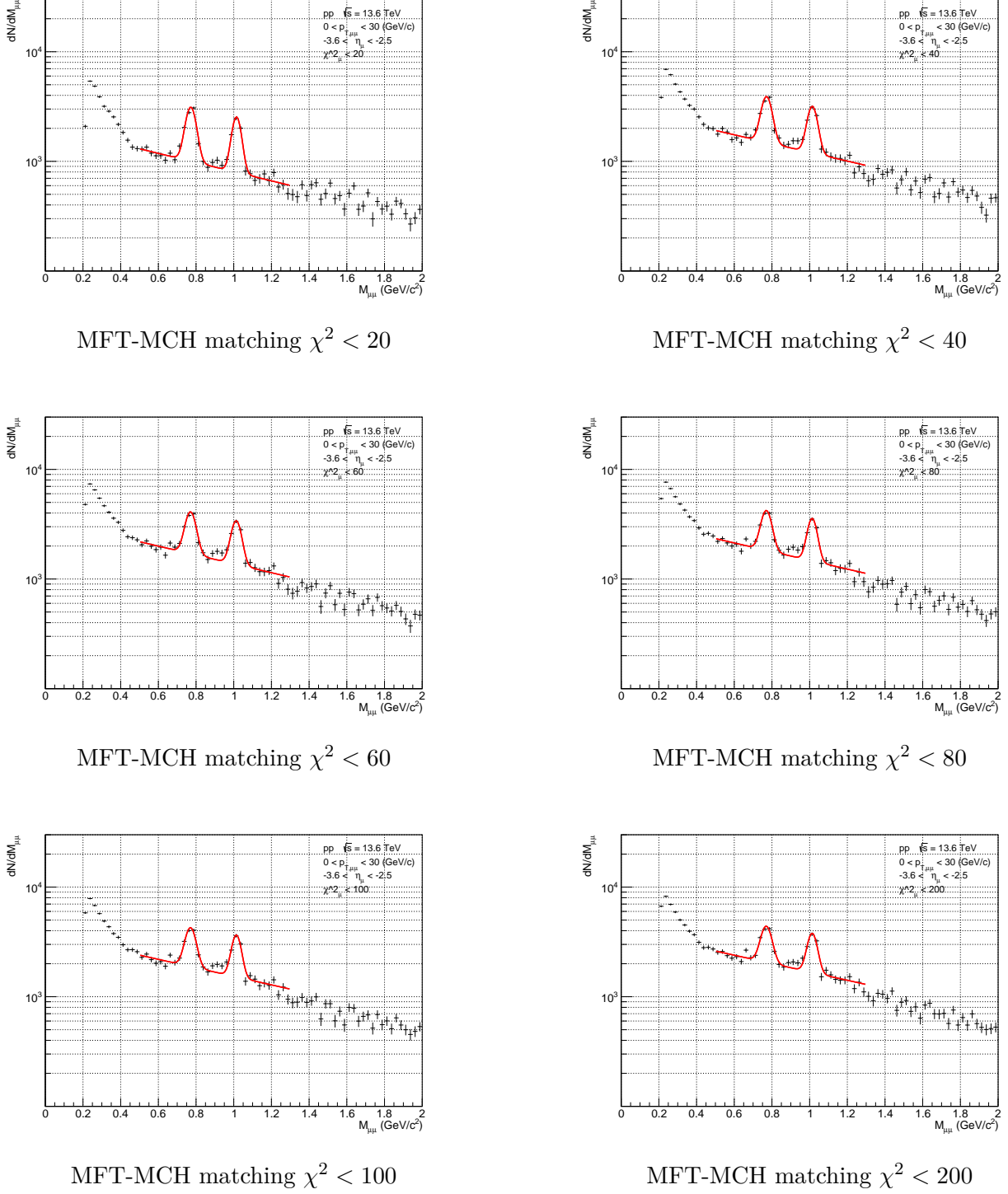


Figure 19: Results of fitting to the correlated invariant mass distribution obtained from Figure 18 in the region  $0.5 < M_{\mu\mu} < 1.3(\text{GeV}/c^2)$ . The red line results from the global fit with (41).

Figure 20 and Figure 21 show the  $\chi^2$  dependence of  $S/\sqrt{S + BG}$  obtained in the fit. The horizontal axis represents the matching  $\chi^2$ , while the vertical axis shows  $S/\sqrt{S + BG}$ . As the cut value is reduced, the value of  $S/\sqrt{S + BG}$  increases. When a cut of  $\chi^2 < 30$  is applied,  $S/\sqrt{S + BG}$  reaches its maximum for both  $\omega$  and  $\phi$ . From this result, it is evident that the optimal matching  $\chi^2$  value is

$\chi^2 < 30$ .

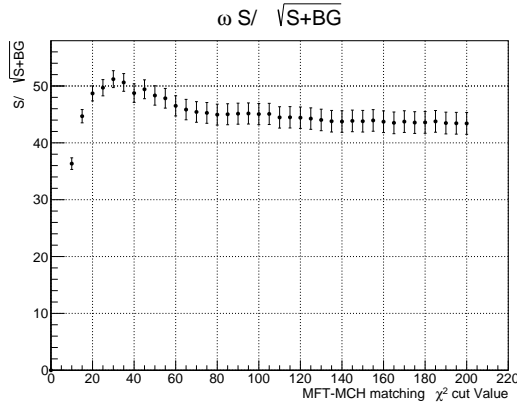


Figure 20:  $\omega$  significance

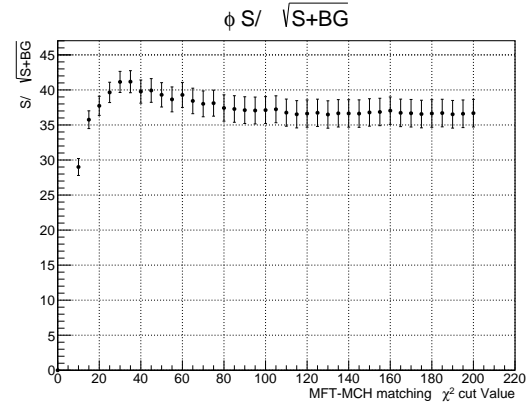


Figure 21:  $\phi$  significance

### 3.6.2 Fake match track removal analysis of Global Track using MFT Track $\eta$ - MCH Track $\eta$

The  $\eta$  distribution of Global Tracks differs significantly from the true distribution. This discrepancy arises due to muon reconstruction involving the MFT, indicating issues with MFT-MCH matching. Fake matches contribute to this significantly distorted  $\eta$  distribution. By removing these distortions, it is shown that the resolution of  $\eta$ ,  $p_T$ , and  $\phi$  for single muons improves. In this analysis, Fake matches are removed by utilising the difference in  $\eta$  between the MFT Track and MCH Track that constitute the Global Track. The dataset used is LHC24b1, which consists of Monte Carlo data of  $pp$  collisions at  $\sqrt{s} = 13.6$  TeV from minimum-bias events. This simulation data has been compared with real data, confirming that they exhibit the same behaviour.

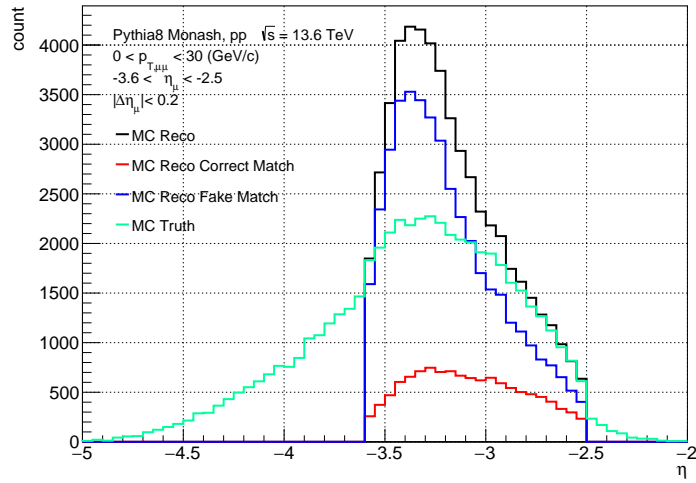


Figure 22: Black is the  $\eta$  distribution of Global Track, red is the  $\eta$  distribution of correct match tracks, and blue is the  $\eta$  distribution of fake match tracks. Moreover, green is the true  $\eta$  distribution corresponding to black.

Figure 22 shows the  $\eta$  distribution of Global Tracks for all  $p_T$  regions. The black histogram represents the reconstructed  $\eta$  distribution of Global Tracks. The blue histogram corresponds to the  $\eta$  distribution of reconstructed tracks identified as Fake matches, while the red histogram represents

the  $\eta$  distribution of correctly matched tracks. The green histogram represents the true  $\eta$  distribution corresponding to the black reconstructed tracks. Comparing the black reconstructed muon distribution with the green true distribution, the acceptance range of Global Tracks is  $-3.6 < \eta < -2.5$ . However, in the green distribution, muons with  $\eta$  values smaller than  $-3.6$  are reconstructed within the  $-3.6 < \eta < -2.5$  range. This phenomenon is likely caused by muons that passed through the absorber and subsequently traversed the MCH-MID system while being outside the MFT acceptance. To remove such tracks, a  $\Delta\eta$  cut is applied as (45).

$$\Delta\eta = \text{MFT Track } \eta - \text{MCH Track } \eta \quad (45)$$

For each track,  $\Delta\eta$  was calculated. Figure 23 shows the distribution. The black represents the distribution of reconstructed muons, the blue represents the distribution of Fake match tracks, and the red represents the distribution of Correct match tracks.

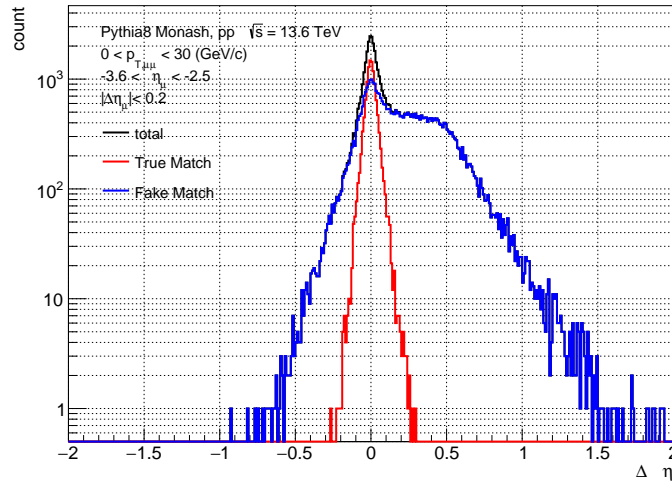


Figure 23:  $\Delta\eta$  distribution of Global Track. Black is the  $\Delta\eta$  distribution of the reconstructed Global Track, red is the  $\Delta\eta$  distribution of the tracks that are correct matches among them, and blue is the  $\Delta\eta$  distribution of the tracks that are fake matches.

For  $|\Delta\eta| > 0.2$ , Fake Match tracks dominate. The distributions and resolutions of each physical quantity are shown by applying a  $|\Delta\eta| < 0.2$  cut to remove Fake matches while retaining as many Correct matches as possible.

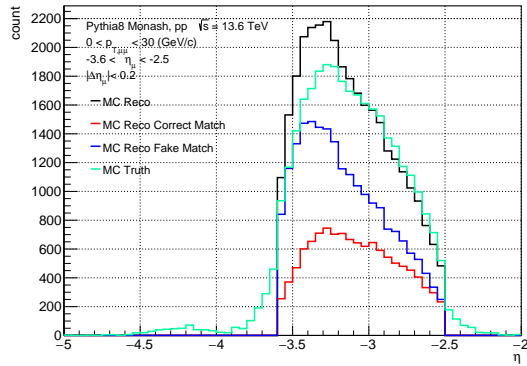


Figure 24: The  $\eta$  distribution of Global Tracks after the  $\Delta\eta$  cut

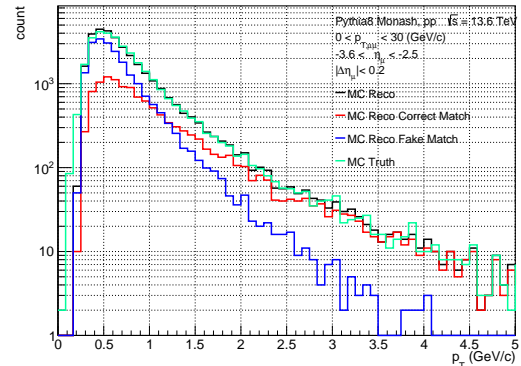
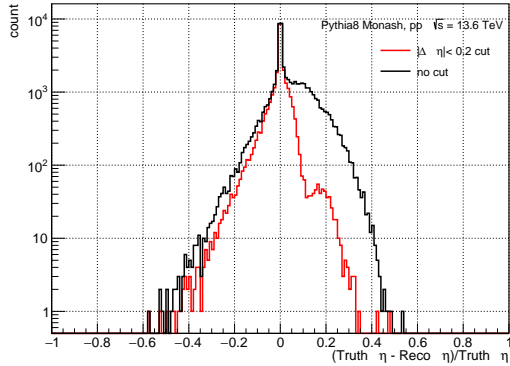
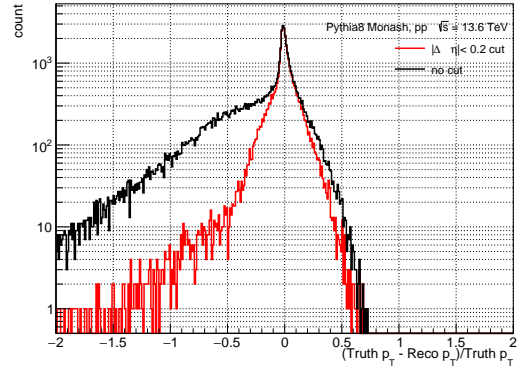
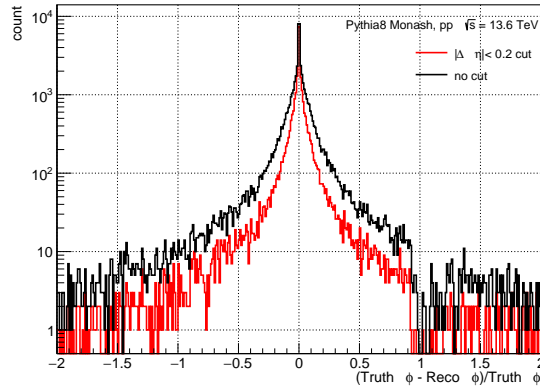
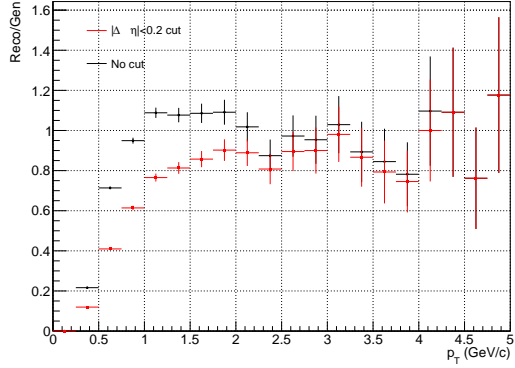
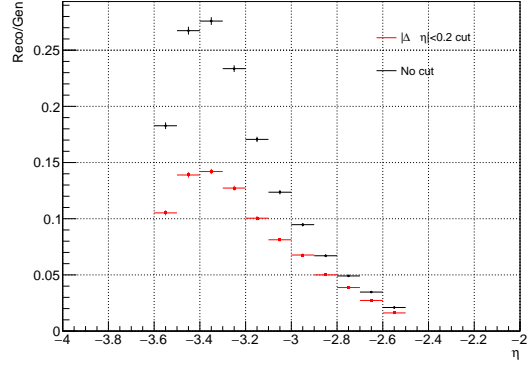
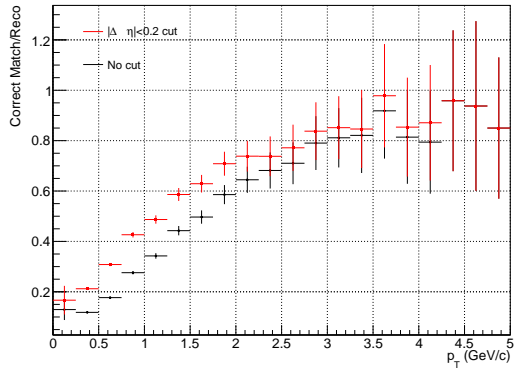
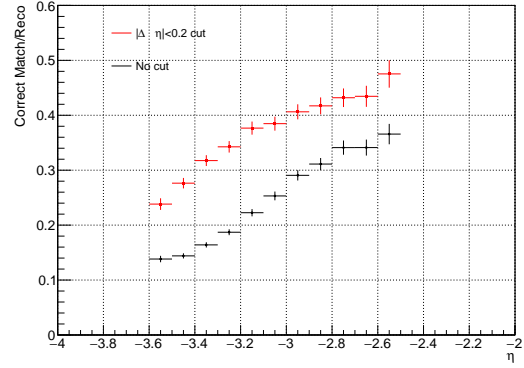
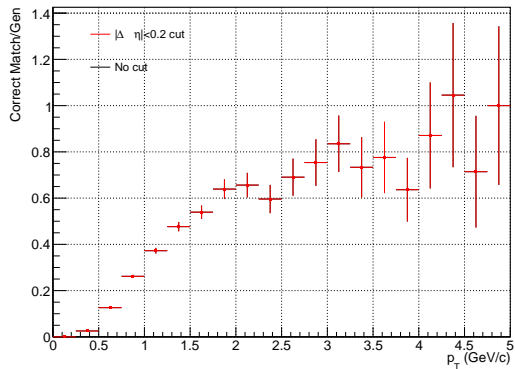
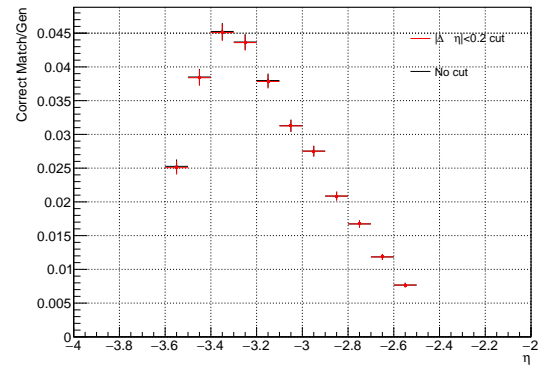


Figure 25: The  $p_T$  distribution of Global Tracks after the  $\Delta\eta$  cut

Figure 24 shows the  $\eta$  distribution after the  $\Delta\eta$  cut. Additionally, Figure 25 displays the  $p_T$  distribution after the  $\Delta\eta$  cut. As in Figure 22, the black histogram represents all reconstructed muon tracks, the red represents Correct match tracks, and the blue represents Fake Match tracks. The green histogram corresponds to the true  $\eta$  distribution for the black muons. Comparing the green distribution of  $\eta$  after the cut with Figure 22, we see that the muons distributed at  $\eta < -3.8$  have been removed. Furthermore, this cut removes many Fake match tracks in the range of  $-3.6 < \eta < -3.2$ . However, as seen from Figure 25, Fake matches originating from low transverse momentum remain.

Figure 26: Resolution of  $\eta$ Figure 27: Resolution of  $p_T$ Figure 28: Resolution of  $\phi$ 

Figures 26, 27, and 28 show the resolution of  $p_T$ ,  $\eta$ , and  $\phi$ , respectively. The horizontal axis represents the resolution, calculated by subtracting the reconstructed quantity from the true physical quantity and dividing it by the true value. The vertical axis represents the count. The black distribution shows the resolution without applying the  $\Delta\eta$  cut, while the red distribution shows the tracks after applying the  $|\Delta\eta| < 0.2$  cut. By comparing the black and red histograms, it is clear that the resolution has a small value for all distributions. This shows that the resolution improves with the cut. Next, we will describe the efficiency and matching purity improvements due to the cut. The  $|\Delta\eta| < 0.2$  cut was applied in such a way as to discard as few correct match tracks as possible while removing fake match tracks. For the  $p_T$  distribution, the efficiency drops below 2 GeV, but the matching purity improves. The product of efficiency  $\times$  purity remains unchanged compared to before the cut. This indicates that the cut does not significantly remove correct matches. For the  $\eta$  distribution, efficiency is reduced in the range  $-3.6 < \eta < -3$ , but matching purity improves in

Figure 29: Efficiency of  $p_T$ Figure 30: Efficiency of  $\eta$ Figure 31: Purity of  $p_T$ Figure 32: Purity of  $\eta$ Figure 33: Efficiency  $\times$  Purity of  $p_T$ Figure 34: Efficiency  $\times$  Purity of  $\eta$

the range  $-4 < \eta < -2$ . Similarly, the product of efficiency  $\times$  purity for  $\eta$  also remains unchanged compared to before the cut.

## 4 Results and Discussion

This chapter presents the graphs of the  $\omega$  and  $\phi$  yields calculated in 2 as the conclusion. Figures 35

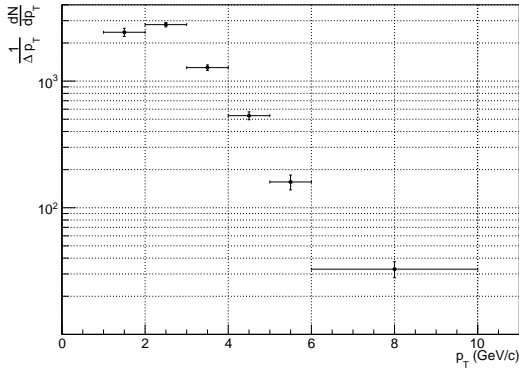


Figure 35:  $\omega$  yield

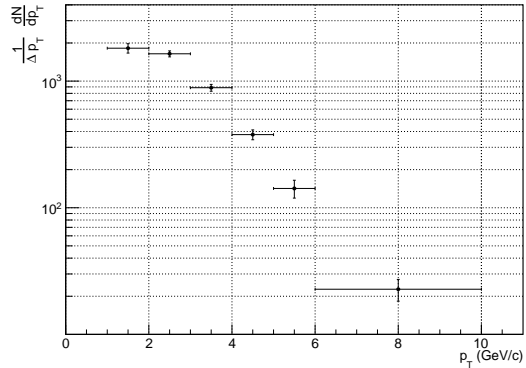


Figure 36:  $\phi$  yield

and 36 show the transverse momentum spectra of the production yields of  $\omega$  and  $\phi$ . The horizontal axis represents the transverse momentum of  $\omega$  and  $\phi$ , while the vertical axis represents the number of counts. Since these spectra are uncorrected, no physical discussion can be made. However, it is observed that the yields decrease as the transverse momentum increases. This behaviour resembles the  $p_T$  spectrum of  $\phi$  production cross-sections measured using forward dimuons in Run 2. Although the  $p_T$  spectrum of  $\omega$  production cross-sections has not been published, the present results exhibit a similar trend to those measured in Run 2. Here, it is necessary to consider the contribution of  $\rho \rightarrow \mu\mu$ . The  $\rho$  meson has a mean mass of  $m = 775.26$  MeV and a full width of  $\Gamma = 149.1$  MeV, leading to a broader distribution than  $\omega$ , which is located at a very similar mass position. Given that the signal extraction method used in this analysis accounts for the broad width of the  $\rho$ , it is considered that the peak structure of  $\omega$  is not significantly affected. As a prospect, improving the resolution of single-muon kinematic variables will enhance the mass resolution, making the  $\omega$  peak sharper and allowing better separation between the  $\rho$  and  $\omega$  peaks. Additionally, by applying acceptance-efficiency corrections using the forward detector system for  $\omega \rightarrow \mu\mu$  and  $\phi \rightarrow \mu\mu$  dimuon reconstruction, the integrated luminosity can be determined from the event counts. This will enable the calculation of production cross-sections from the present results, allowing for direct comparison with Run 2 results.

Discuss single muon track reconstruction, 3.6, and prospects. In the current muon track reconstruction algorithm, the  $\eta$  and  $\phi$  of the muon are determined using the MFT Track to improve their precision. However, the DCA is calculated using parameters obtained from the global fit of the Global Track. Since using tracks closer to the collision point allows for more precise measurements unaffected by the absorber, it is expected that the accuracy of the DCA measurement can be improved by using the parameters of the MFT track that constitutes the Global Track. Furthermore, improvements in MFT-MCH matching are also needed. As seen in Figure 31, the matching purity significantly decreases at low transverse momentum ( $p_T$ ). This degradation occurs because low- $p_T$  muons undergo multiple scattering and energy loss in the absorber, making MFT-MCH matching more challenging. However, this study demonstrated that applying a  $\Delta\eta$  cut improves matching purity in the low- $p_T$  region. This result suggests that continued analysis can further enhance matching purity.

The ultimate goal is to measure the changes in the mass distribution of light vector mesons in lead-lead collision events. This study has revealed several remaining challenges, including issues with matching purity at low transverse momentum and the development of the track reconstruction algorithm. Another challenge is improving the quality of muon tracks in high-multiplicity events in heavy-ion collisions. As a first step, efforts will be focused on improving matching purity and developing the track reconstruction algorithm in proton-proton collisions, where the event multiplicity is relatively low. Subsequently, similar improvements will be pursued in heavy-ion collisions. Going forward, the aim is to clarify the changes in the mass distribution of light vector mesons due to QGP formation and observe the restoration of chiral symmetry.

## 5 Summary

In this study, we analyzed forward muon pairs in ALICE from  $\sqrt{s} = 13.6$  TeV  $pp$  collisions. The peaks corresponding to  $\omega \rightarrow \mu\mu$  and  $\phi \rightarrow \mu\mu$  in the dimuon mass distribution were extracted with Gaussian functions. In contrast, other components were fitted with an exponential function. These analyses were performed for each transverse momentum range, and the transverse momentum spectra of  $\omega$  and  $\phi \rightarrow$  yields were presented. Additionally, an analysis was conducted to improve the purity of the matching MFT and MCH. By applying a cut on the difference in  $\eta$  between the MFT Track and the MCH Track that constitute the Global Track, we demonstrated the ability to remove Fake match tracks. Furthermore, the optimal MFT-MCH matching  $\chi^2$  cut was determined using the signal yields of  $\omega$  and  $\phi$ . As a prospect, further improvements in the quality of single muon tracks will be pursued. Ultimately, this study aims to clarify the changes in the mass distribution of light vector mesons caused by the formation of the QGP in lead-lead nuclear collisions.

## 6 Acknowledgements

I want to thank everyone involved in this study. First of all, Dr. Shigaki, thank you very much for not only your daily guidance but also for giving me various opportunities to present my research and to learn at research meetings and academic conferences. Those experiences helped me gain basic knowledge of the ALICE experiment and of heavy ion collision experiments as a whole. Dr. Yamaguchi. Thank you very much for all your comments on the plots during the analysis process, especially at the meeting. Thanks to your help, I developed my ability to think logically and proceed with my research, even though it is still in its infancy. Dr. Yano, thank you very much for your opinions on muon analysis. I learned the importance of thinking about the analysis necessary for current muon analysis and planning for the future. Dr. Homma, Dr. Miyoshi, thank you very much for your questions and suggestions in the weekly lab meetings, business trip reports, midterm presentations, and so on. Through your questions and suggestions, I learned about your attitude toward research. Mr. Oya, thank you very much for teaching me the method of forward muon pair analysis from scratch. Your wide-ranging opinions, from consultation on research policy to debugging the analysis code, helped me advance my research. As a senior student with the highest grade in the laboratory, I have had many occasions to learn from you. Mr. Kimura, thank you very much for consulting with me on many aspects of my research policy. Your knowledge of the theory of lepton pair measurement has greatly advanced my understanding of this research. To everyone in the laboratory: Thank you for your daily involvement, from opinions about the contents of this research

to refreshing chats. Bator, Maurice, Sarah, and Steffer for their appropriate comments during my presentations at the MFT meeting and the DQtoMuMu PAG meeting. These comments helped me understand what was missing in my analysis and what I needed to think about.

To the ALICE experimental group. This study was analyzed using data acquired by the ALICE experimental group. Once again, I would like to express my gratitude.

## References

- [1] S. Navas *et al.* [Particle Data Group], Phys. Rev. D **110**, no.3, 030001 (2024) doi:10.1103/PhysRevD.110.030001
- [2] W. Weise, Nucl. Phys. A **553**, 59C-72C (1993) doi:10.1016/0375-9474(93)90615-5
- [3] A. Maire, "Phase diagram of QCD matter: Quark-Gluon Plasma," 2015. Available at: <https://cds.cern.ch/record/2025215>
- [4] ALICE Collaboration., Acharya, S., Adamová, D. et al. The ALICE experiment: a journey through QCD. Eur. Phys. J. C 84, 813 (2024). <https://doi.org/10.1140/epjc/s10052-024-12935-y>
- [5] F. Geurts and R. A. Tripolt, Prog. Part. Nucl. Phys. **128**, 104004 (2023) doi:10.1016/j.ppnp.2022.104004 [arXiv:2210.01622 [hep-ph]].
- [6] S. Acharya *et al.* [ALICE], [arXiv:2308.16704 [nucl-ex]].
- [7] R. Rapp and J. Wambach, Adv. Nucl. Phys. **25**, 1 (2000) doi:10.1007/0-306-47101-9\_1 [arXiv:hep-ph/9909229 [hep-ph]].
- [8] S. Damjanovic *et al.* [NA60], Nucl. Phys. A **783**, 327-334 (2007) doi:10.1016/j.nuclphysa.2006.11.015 [arXiv:nucl-ex/0701015 [nucl-ex]].
- [9] "Technical Design Report for the Muon Forward Tracker," CERN-LHCC-2015-001, ALICE-TDR-018, 2015. Available at
- [10] "ALICE dimuon forward spectrometer: addendum to the Technical Design Report" CERN-LHCC-2000-046, Technical design report. ALICE, 2000. Available at <https://cds.cern.ch/record/494265>